

This is an Open Access document downloaded from ORCA, Cardiff University's institutional repository: <https://orca.cardiff.ac.uk/id/eprint/109621/>

This is the author's version of a work that was submitted to / accepted for publication.

Citation for final published version:

Omosanya, Kamaldeen O., Eruteya, Ovie E., Siregar, Einstein S.A., Zieba, Krzysztof J., Johansen, Ståle E., Alves, Tiago and Waldmann, Nicolas D. 2018. Three-dimensional (3-D) seismic imaging of conduits and radial faults associated with hydrothermal vent complexes (Vøring Basin, Offshore Norway). *Marine Geology* 399 , pp. 115-134.
10.1016/j.margeo.2018.02.007

Publishers page: <http://dx.doi.org/10.1016/j.margeo.2018.02.007>

Please note:

Changes made as a result of publishing processes such as copy-editing, formatting and page numbers may not be reflected in this version. For the definitive version of this publication, please refer to the published source. You are advised to consult the publisher's version if you wish to cite this paper.

This version is being made available in accordance with publisher policies. See <http://orca.cf.ac.uk/policies.html> for usage policies. Copyright and moral rights for publications made available in ORCA are retained by the copyright holders.



Three-Dimensional (3-D) seismic imaging of conduits and radial faults associated with hydrothermal vent complexes (Vøring Basin, Offshore Norway)

Kamaldeen O. Omosanya¹; Ovie E. Eruteya²; Einstein S.A. Siregar¹; Krzysztof J. Zieba¹, Ståle E. Johansen¹; Tiago M. Alves³; Nicolas D. Waldmann²

¹Department of Geoscience and Petroleum, Norwegian University of Science and Technology, Norway.

²Dr. Moses Strauss Department of Marine Geosciences, Leon H. Charney School of Marine Sciences, University of Haifa, Israel.

³3D Seismic Laboratory, Cardiff University, United Kingdom.

Corresponding author: kamaldeen Omosanya (kamaldeen.o.omosanya@ntnu.no)

Abstract

Here, we document a suite of radial faults associated with hydrothermal vent complexes in the Vøring Basin, offshore Norway. These complexes have pyramid-shaped, cylindrical- and conical-shaped conduits, with a dome-, or eye-shaped morphology at their summit, intruding on Paleogene sedimentary rocks. Hydrothermal vents are intimate with the tips of magmatic sills that were emplaced at depths ranging between 1800 and 5800 ms Two Way Travel Time (TWTT). At shallower depths of 1800 to 3000 ms TWTT and intermediate depths of 3000 to 5000 ms TWTT, magmatic sills regularly intersect the lower parts of the vent conduits, which are characterized here as pipes. An important parameter that is used to characterize the morphology of a hydrothermal vent conduit is the width of the conduit, which is defined as the longest axis marking the extent of the vents' conduit within the surrounding host-rock strata. Our findings reveal that radial faults are commonly associated with the summits of hydrothermal vents, implying the existence of local stress fields around the vents, where the maximum compressive stress is radial and minimum stress is circumferential, which overrides the regional stress field and indicate variable stress regimes as opposed to tectonic faults. Importantly, circumferential stretching due to catastrophic plumbing of hydrothermal fluids, differential compaction and intensive fracturing enabled the polygonal faults to realign in a radial pattern resulting in the formation of radial faults at the vent summit. As a corollary of this work, we hypothesize that pyramid-

shaped hydrothermal conduits are possibly markers of protracted sill emplacement in sedimentary basins.

Keywords: Magmatic sills, hydrothermal vents, fluid flow, radial faults, 3-D seismic data, Vøring Basin.

1. Introduction

Hydrothermal vent complexes are consequences of magmatic intrusions in sedimentary basins occurring across large igneous provinces (Hansen, 2006; Jamtveit et al., 2004; Planke et al., 2005; Svensen et al., 2003). Generic models have shown that hydrothermal vent complexes arise from the expulsion of gases and fluidized materials associated with the emplacement of magmatic sills e.g., (Jamtveit et al., 2004; Svensen et al., 2006). During this process, substantial amount of gases are released to the atmosphere or hydrosphere e.g., (Aarnes et al., 2012; Jamtveit et al., 2004) and have been invoked as contributors to global warming during the Paleocene Eocene Thermal Maximum (PETM) (Reynolds et al., 2017; Svensen et al., 2004). Hydrothermal vents complexes usually originate from the tip of magmatic sill complexes as a result of intensive fracturing of the supra-sill stratigraphy arising from overpressure build-up associated with the release of fluids and gases within the metamorphic aureoles (Aarnes et al., 2012; Iyer et al., 2017; Jamtveit et al., 2004).

Seismic reflection data, both two-dimensional (2-D) and three-dimensional (3-D) have revolutionized our understanding of the architecture of hydrothermal vent complexes, their origin and interaction with magmatic sills, and focused fluid-flow (Planke et al., 2005; Svensen et al., 2006). Seismic data have permitted the visualization of the true dimensionality of these features at resolutions of tens of meters (Alves et al., 2015; Hansen and Cartwright, 2006; Planke et al., 2005; Smallwood and Maresh, 2002; Svensen et al., 2006). On seismic reflection data, hydrothermal vent complexes are manifested as pipe-like and vertical zones of low amplitude and chaotic reflections in the lower parts and terminating as dome-, eye- or crater-like morphologies at the summit (Hansen, 2006; Svensen et al., 2007). Importantly, these vents can be re-used as fluid flow conduits after formation (Holford et al., 2017). Previous studies have focused on the implication of hydrothermal venting for the timing of intrusive events e.g. (Hansen, 2006), petroleum systems (Aarnes et al., 2015; Iyer et al., 2017) and paleoclimate (Iyer et al., 2013; Iyer et al., 2017; Reynolds et al., 2017; Svensen et al., 2007; Svensen et al., 2004). However, there is a significant gap in our understanding of the interaction between the evolution of the hydrothermal vent complexes and deformation in the supra-sill stratigraphy.

In this work, we document the development of a suite of hydrothermal vent complexes and associated radial faults using three-dimensional (3-D) seismic reflection data from the Vøring Basin, offshore Norway (Figure 1). The relationship between hydrothermal vents and radial faults has never been investigated from seismic data to the best of our knowledge. In parallel, the exact mechanism for

such vent-related radial faulting remains unclear and undocumented, as opposed to radial faults found at the crest of salt structures e.g., (Carruthers et al., 2013; Mattos et al., 2016; Stewart, 2006; Withjack and Scheiner, 1982). These are all crucial for an inclusive understanding of the evolution of hydrothermal vent complexes. Therefore, the objective of this paper is to document and understand the origin of radial faults developed at the crest of several hydrothermal vent complexes in the Vøring Basin. We show, for the first time, high-resolution imagery of distinctive radial fault systems above the summit of hydrothermal vents and used those findings to re-evaluate the mechanism and anatomy of hydrothermal vents in the Vøring Basin.

2. Geological setting of the Vøring Basin

The Norwegian Sea covers most of the continental margin between latitudes 62°N and 69°30'N and is comprised of two principal basins, which are the Vøring and the Møre Basins (Figure 1; Brekke, 2000). The uplifted Norwegian landmass, the Cretaceous Trøndelag Platform to the east, and the Møre and Vøring Marginal Highs and Eocene lavas to the west all flank both basins (Brekke, 2000; Doré et al., 1999; Planke et al., 2005). On a regional scale, the Norwegian margin was tectonically active in Late Palaeozoic until Early Cenozoic times in association with three major tectonic episodes (Doré et al., 1999). The first episode reflected the final closure of the Iapetus Ocean during the Caledonian Orogeny in the Late Silurian to Early Devonian (Brekke, 2000). A second episode was marked by extensional events spanning from the Late Devonian to the Palaeocene that culminated in continental separation between Greenland and Eurasia (Brekke, 2000; Eldholm et al., 1989; Skogseid et al., 1992). A third and final episode reflecting seafloor spreading in the North Atlantic between Eurasia and Greenland occurred from the earliest Eocene to the present (Brekke, 2000).

The Vøring Basin is one of the magmatic basins along the NE Atlantic margin recording pervasive emplacements of magmatic sills and hydrothermal vent complexes (Hansen, 2006; Jamtveit et al., 2004; Planke et al., 2005; Svensen et al., 2006; Svensen et al., 2004). Palaeozoic orogenic events such as the Caledonian Orogeny mainly preconditioned the NE-SW structural trend of the Vøring Basin (Doré et al., 1997). Much of the pre-Cretaceous geology of the Vøring Basin was controlled by extensional events (Bukovics and Ziegler, 1985). Extension dominated in the Early Mesozoic with the development of many basins to the south of the Vøring Basin such as Froan Basin and Halten Terrace (Doré et al., 1999). The Early Cretaceous geodynamic evolution of the Vøring Basin is directly linked to continental break-up and the subsequent opening of the Norwegian and Greenland Seas (Figure 1a). Increased magmatism during the Late Palaeocene resulted in the extrusion of flood basalts in the northwestern segment of the study area (Eldholm et al., 1989; Skogseid et al., 1992). Pervasive magmatism followed the latest stage of rifting leading to continental breakup at ~55 Ma (Lundin and

Doré, 2002). This resulted in the emplacement of numerous dolerite intrusions within Cretaceous (and older) rocks in the study area (Ostendorf and Gundersen, 2003; Skogseid et al., 1992).

The lithostratigraphy of the study area, as revealed by borehole 6707/6-1, spans from the Cretaceous Nise Formation to the Quaternary Naust Formation (Figure 2a). The Nise Formation is a thick unit of predominantly non-calcareous mudstones deposited in open marine environments between the Kvitnos and Springar Formations (Dalland et al., 1988). Rock types within the Nise formation include mudstones with subordinate siltstones, sandstones and occasional carbonate stringers (Dalland et al., 1988). Conversely, the overlying Springar Formation generally comprises a thick, widespread sequence of marine mudstones, limestone, and dolomite, and sandstone stringers occur in this unit (Dalland et al., 1998). The Springar Formation is Maastrichtian to Campanian in age and was deposited in outer-shelf to bathyal environments with restricted water circulation (Dalland et al., 1988).

The Tang Formation comprises dark grey to brown claystone with minor sandstone and limestone that were deposited in a deep marine environment. (Dalland et al., 1988). The base of the Tare Formation is defined by an increase in tuff content (Dalland et al., 1988). The Late Palaeocene Tare Formation is comprised of dark-grey, green or brown claystones with some thin sandstone stringers and variable contents of tuffaceous material (Dalland et al., 1988). The Tang and Tare Formations are part of the Rogaland Group. The overlying group is the Hordaland Group, which comprises the Early Eocene to Early Miocene Brygge Formation. Lithologies within this formation are claystone with stringers of sandstone, siltstone, limestone and marl (Dalland et al., 1988; Deegan and Scull, 1977). The Nordland Group that, in this location, consists of Kai and Naust formations overlies the Hordaland Group. The Kai Formation of Early Miocene to Late Pliocene age is comprised of alternating claystone, siltstone and sandstone with limestone stringers deposited in marine environments (Dalland et al., 1988; Eidvin et al., 1998). The Naust Formation is Late Pliocene in age and was deposited in a marine environment (Dalland et al., 1988). Lithologies within the Naust Formation include interbedded claystone, siltstone and sand, occasionally with very coarse clastics in the upper part (Eidvin et al., 2013).

3. Datasets and methods

In this study, we interpreted a time migrated, three-dimensional (3-D) seismic reflection data covering approximately 820 km² of Naglfar Dome in the Vøring Basin (Figure 1). The inlines and cross-lines of the seismic survey are oriented in N-S and E-W directions, with bin spacing of 25 m and 12.5 m, respectively. The seismic cube has a vertical extension of 8 s with vertical sampling rates of 4 ms. The seismic cube is displayed in the European or reverse SEG (Society of Exploration Geophysicist) polarity convention, whereby a downward increase in acoustic impedance represents a trough (blue colour). A downward decrease in acoustic impedance denotes a peak (red colour). The vertical seismic resolution of the seismic dataset is ~13.75 m across the Tang and Brygge Formations. Using an average

velocity of 2200 m/s taken from borehole 6706/6-1, and a dominant frequency of 40 Hz. Importantly, that interval velocity value adopted here is not likely representative of the hydrothermal vent complexes due to, for example brecciation, and cementation. The horizontal resolution is equal to the bin spacing.

The seismic interpretation include interpretation of ten horizons (H1 to H10), with particular emphasis on two formation tops (the Brygge and Tang Formations) and several arbitrary horizons marking the tops and bases of the hydrothermal vents, i.e., TV and BV, twenty-five (25) magmatic sills, twenty-two (22) hydrothermal vent complexes, one-hundred and five (132) tectonic faults and fifty-three (53) radial faults. Prior to the seismic interpretation, the original seismic cube was converted to a structurally smoothed cube. Structural smoothing is a volume attribute that reduces the number of geophysical artefacts in a seismic cube and improve the resolution of the initial seismic cube. Hence, applying a spatial filter removes noise from seismic data while preserving important geometric characteristics and discontinuities (Ngeri et al., 2015; Zervas et al., 2018).

Magmatic sills were interpreted based on their amplitude character, geometries and lateral continuity within the host-rock strata. Magmatic sills can have remarkable seismic stratigraphic expression with the host-rock strata as they usually show local transgression across stratigraphic levels, restricted lateral continuity and or/crosscut the host-rock strata (cf. Planke et al., 2000). In addition, their high seismic amplitude is a reflection of greater densities and seismic velocities between the magmatic sills and their host-rock strata. These physical differences result in high acoustic-impedance contrasts at the sill–host rock contacts (Smallwood and Maresh, 2002), which reflect more seismic energy back to the surface than the low impedance boundaries typically occurring between sedimentary rocks (Brown, 2004). Magmatic sills and other igneous bodies are consequently expressed as high-amplitude reflections on seismic data (Planke et al., 2005; Smallwood and Maresh, 2002). Hence, magmatic sills in this work are seismic anomalies comprise of localized brightening of positive amplitude reflections, or partial loops of ‘peak-trough-peak’ reflections similar to the sea floor reflection (Alves et al., 2015; Omosanya et al., 2016; Omosanya et al., 2017).

Hydrothermal vent complexes are interpreted on seismic sections based on the morphologies of their upper parts and conduit zones. In addition to the identification and interpretation of hydrothermal vent complexes, a novel statistical parameter called conduit width is introduced here to discriminate the different conduits. Conduit width represents the longest axis corresponding to the maximum extent of the conduit zone within the host-rock strata as expressed in map view (Figures 2c). Statistical analyses related to hydrothermal vents’ geometries include plots of conduit width with depth to distinguish pyramidal-shaped conduits from conical-shaped and cylindrical-shaped ones. In this paper, ‘ R^2 ’ and ‘ R ’ are the coefficients of determination and correlation between these parameters i.e., the degree to which the vent conduit width is dependent on depth. Bar charts were also made to show the range of area and length for the magmatic sills. Additionally, faults were interpreted across seismic sections perpendicular to fault strike (Mansfield and Cartwright, 1996). First, the tectonic faults were

individually mapped, and their trends displayed on structural plots and a map of the H8 horizon to understand the interaction between them and the other faults in the study area. The structural plots used in this work include rose diagrams and equal area projections to display fault attitude such as strike and angle of dip. Secondly, the radial faults were interpreted using combined variance time slices and seismic sections as explained below.

To validate the location of hydrothermal vents and faults interpreted on seismic sections, seismic attribute maps and time-slices of variance and chaos were further used (Figure 3). Hydrothermal vents were mapped out on the time-slices, while their conduits' widths within the host-rock strata were estimated from the interfered root zones to their summits. Radial faults above the vents' summits and their associated conduit zones were also described in detail and highlighted using variance, chaos and local structural dip seismic attribute. The variance attribute is a direct measurement of dissimilarity between seismic traces and converts a volume of continuity into a volume of discontinuity, highlighting structural and stratigraphic boundaries (Brown, 2004). Variance seismic attribute is also a good discriminator of lithology types. The chaotic facies associated with hydrothermal vents as a result of the disruption of the originally stratified sedimentary rock during fluid expulsion were mapped as features with low variance coefficients and zones of dim to chaotic reflections relative to the well-bedded, high-medium amplitude facies of the host-rock strata (see Jamtveit et al., 2004). Similarly, faults represent trace-to-trace variability and were mapped as features with high variance coefficients. The chaos attribute was used to map out the geometries of the hydrothermal vents. The chaos attribute effectively maps the chaotic signal pattern contained within a unit of seismic data and measures the "lack of organization" in the dip and azimuth estimation method associated with fluid migration pathways and intrusions (Mohammedyasin et al., 2016). The local structural dip attribute is an edge detection method for structures characterized by local changes in dip e.g., faults, channels and salt diapirs (Marfo et al., 2017). This seismic attribute is applicable for visualizing vent conduits with high dip values compared to the surrounding host-rock strata.

4. Observations and interpretations

4.1 Interpreted seismic horizons

The ten (10) main horizons interpreted in the work are labelled H10 to H1 from oldest to youngest (Figures 2). Significantly, horizons H5 to H9 provide an important indication of the timing of fluid venting in the study area. Horizon H9 is a faulted, low to moderate amplitude reflection that overlies the Tang Formation (Figure 2a). Furthermore, H8 is intra Brygge Formation in wellbore 6706/6-1 and is reflected as a low to moderate amplitude, discontinuous reflection that is regularly intersected by polygonal faults and hydrothermal vents (Figure 2a). Horizon H7 lies above most of the hydrothermal

vents and is a discontinuous moderate to high amplitude reflection (Figure 2a). Both horizons H6 and H5 are part of the Kai Formation (Figure 2a) and vary from low to moderate amplitudes to high amplitude reflections. In addition to these horizons, few arbitrary horizons were interpreted across the seismic cube and are used to mark the upper boundary of the hydrothermal vents. Horizon TV represents the termini of all the vents, whereas BV is the base horizon (Figure 2a).

4.2 Interpretation of hydrothermal vent complexes

Twenty-two (22) hydrothermal vent complexes were interpreted in the study area and were developed at two principal stratigraphic formations, the Brygge and Tang Formations (Figures 2 to 8). The anatomies of hydrothermal vent complexes are described according to several previous works e.g., (Hansen, 2006; Hegglund, 1998; Planke et al., 2005). In the study area, the hydrothermal vent complexes are characterized by (a) a root zone (b) an intermediate zone i.e., the conduits and (a) an upper zone/ a vent (Figure 3). Variance time slice is a quick look tool that allows the direct identification of the root, conduit and vent zones (Figure 3). On seismic sections and variance time slices, the root zone was inferred as the deepest extent of the chaotic, altered, distorted, and low amplitude reflections of the conduit zone (Figure 3). The areas of intermediate to high variance coefficients, which distinctly contrast with the surrounding host-rock strata of low variance coefficients, mark the conduit and vent zones on the variance time slices (Figures 3 and 4a). On maps and time slices, the vents are circular to elliptical zones and their morphologies on seismic sections are revealed as either eye-shape or dome-shape structures (Figure 2b; Planke et al., 2005). The dome-shaped vents are the most common and have mound structures at their tops (Table 1). This arises from the expulsion of hydrothermal fluids and fluidized sediments on the seafloor or paleo seafloor. Subsequent build-up of the entrained sediments on the seafloor results in the dome-like and eye-like end-members (Mazzini et al., 2006; Planke et al., 2005).

In addition, the description of the basal relationship, overburden relationship and internal geometries of the vents follows the scheme of Hansen (2006) and Planke et al. (2005). For most vents, the internal geometry includes chaotic and downlapping reflections (Figures 5 to 7), whereas their basal relationship varies mostly from being truncational (e.g., V2, V4, V11, and V15) to downwarped concordant (V7). In contrast, dome-shaped vents have flat-lying bases that are concordant with the underlying strata and upward doming (mounded) upper boundaries. The heights of some of the mounds can reach a maximum of approximately 220 ms TWTT (Figures 2b and 5a). Additionally, hydrothermal vents in the study area show disparate relationships with their overburden strata at the Top Vent horizon (TV). These include divergent reflections below the TV horizon (V7, Figure 5a), concordant reflections (V19, Figure 5b) and onlapping reflections or relationships (V2, Figure 7). At their upper parts, smaller magmatic sills and faults sometimes crosscut the vents (Figure 7). This is particularly true for some of the dome-shaped vents, which frequently show faults at their upper parts, while other vents occasionally

have folds associated with their summits (Figures 5a, 6b- 6d). Such folds at the vents' summit can have wavelengths reaching up to approximately 1.5 km and show a seismic stratigraphic relationship of onlap with overlying strata (Figure 6d).

The majority of hydrothermal vents are connected to chaotic and vertically disturbed focused conduits (Figures 5 to 7), which in turn are generally underlain by saucer-shaped magmatic sills (Figures 7a and 7b). Hydrothermal vent conduits can extend from approximately 2500 to 5000 ms TWTT, affecting the entire Paleogene sequence (Figures 5 to 7). Geometrically, the vents' conduits include cylindrical-, conical- and pyramid- shapes on seismic sections (e.g., Figures 5b, 6 and 7). Pyramid-shaped conduits are wider at the base and thinner at the crest (Figure 7). Conversely, conical-shaped conduits are wider at the top, close to the vents, and thinner at their bases (e.g., Figures 5c and 6b), while the cylindrical-shaped conduits are almost tube shaped from top to base (Figure 5b).

To distinguish the different types of hydrothermal conduits in our study area, we followed a statistical approach to assess the relationship between their widths and depths, and present the three common relationships observed. Pyramid-shaped hydrothermal conduits generally show a positive correlation between their widths and depths e.g., V2 (Figure 8a, Table 1). The coefficient of determination (R^2) and correlation (R) can reach up to 0.924, showing a near perfect positive correlation between the two parameters. At shallow depths, the pyramid-shaped conduits have widths that are smaller compared to deeper depths, where the widths are larger (Figures 7 and 8a). Deviations from this trend are observed at intermediate depths, where the value of 'w' for the hydrothermal vent complexes can become larger than that observed in both shallow and deeper strata (Figures 7d and 7e). In contrast, conical-shaped conduits show a negative correlation between their widths and depths e.g., V18 (Figures 6b and 8b). The values of R^2 and R can reach up to 0.966 (Figure 8b, Table 1). For cylindrical-shaped conduits, the 'w' is almost equal from top to base, showing low coefficients of correlation, e.g., V19 (Figure 5b). There, the coefficient of correlation is low, with a value of 0.366 (Figure 8c, Table 1). Hence, pyramid-shaped conduits have increasing 'w' with depth, conical-shaped conduits have inverse trend for 'w' with depth, and cylindrical-shaped conduits have almost constant 'w' with depth.

4.3 Magmatic sills associated with hydrothermal vent complexes

Twenty-five (25) magmatic sills that are associated with the hydrothermal vents are reflected as seismic anomalies with signals that are similar to the seabed reflection i.e., complete or partial loops of 'peak-trough-peak' reflections (Alves et al., 2015). The sills are positive high amplitude anomalies that contrast remarkably with the surrounding host rock strata of low amplitude (Figures 6d, 7a, 7b, 9a and 9b). Apart from their high amplitude character, the magmatic sills show abrupt lateral terminations and complex geometries. All these characters fit archetypical magmatic sills described from seismic reflection data (Hansen and Cartwright, 2003; Hansen, 2006; Planke et al., 2005), which have been

confirmed in a number of studies from borehole data (Grove, 2013; Hansen and Cartwright, 2006; Jackson et al., 2013; Omosanya et al., 2016; Planke et al., 2005; Thomson and Hutton, 2004), outcrop data (Muirhead et al., 2014; Walker et al., 2017) and synthetic seismic forward models (Eide et al., 2017; Magee et al., 2015).

The interpreted magmatic sills also show close associations with different seismic features (Figures 9a and 9b). These include underlying zones of disrupted seismic signals, which possibly indicate the presence of fluids. Furthermore, acoustic blanking zones (ABZ) beneath the sills signify the differences in acoustic properties and reflectivities between the sills and their underlying sedimentary rocks. Hence, there is a decrease in acoustic impedance contrast from the sills above to the strata below, and vertical zones of disrupted seismic reflection/pipes are found adjacent to some sills. The latter pipes are rooted within the areas of acoustic blanking where sills are regularly seen (Figure 9a), providing evidence of cause-effect between the pipes and magmatic sills. The interpreted magmatic sills in some cases are also associated with multiple positive high amplitude anomalies that are perhaps magmatic sills under seismic resolution (e.g., Figures 9a and 9b). This is most especially possible when the overburden masks imaging of these sills, as discussed in the works of (Eide et al., 2017).

Nonetheless, at depths of approximately 5000 to 5800 ms TWTT, some of the sills generally trend in the NE-SW direction, forming an interconnected sill complex (Figure 10a). These are categorized as being the deeper sills, which are generally saucer-shaped (Figure 10). Sills at depths of 3000 to 5000 ms are classified as intermediate sills. These include saucer-shaped and transgressive sills e.g., Sills 18 and 25 (Figures 9c and 9d). Shallow sills occur at depths of 1800 to 3000 ms TWTT e.g., Sill 18, and are generally saucer-shaped (Figures 10a). Furthermore, the deeper sills have lengths of approximately 74 to 235 km (mean-124 km) and areas ranging from 96.4 to 345 km² (Figure 11a). Intermediate sills cover areas of 3.45 to 292 km² and are 8.2 to 126 km long (mean of 40 km; Figure 11b). The shallow sills show total areas that range from 14.8 to 73.6 km² and lengths varying from 32.2 to 90.6 km (mean of 46 km; Figure 11c). In terms of magmatic plumbing, the sills generally step towards the northern part of the study area and produced a lateral and extensive chain of sills that covers several 10 s of km in both the NNE-SSW and E-W directions (Figures 10a and 10b).

Flow indicators such as steps show the direction of sill propagation, and in the study area, they include both continuous (Figure 9a) and discontinuous types (Figure 9b). Steps are flow indicators within magmatic sills and are generally oriented parallel to the axis of sill emplacement (Pollard et al., 1975; Thomson and Hutton, 2004). When disconnected, the steps provide evidence of original offset between magma segments at different stratigraphic levels i.e., the inflation of the segments was not sufficient to cause two adjacent steps to coalesce and form a continuous step (Schofield et al., 2012). In addition to steps, most of the sills show pointed bases, indicating that the magma generally flows outward and radiates from a point source or centre (see Thomson and Hutton, 2004).

5. Radial faults at the summits of hydrothermal vents

Radial faults in this work are extensional faults that generally radiate from a central point i.e., vents' summits (Alsop, 1996; Davison et al., 2000; Yin and Groshong Jr, 2003). On seismic sections, the radial faults are normal faults at the summits of the vents (e.g., Figure 3), while they are seen as discontinuities marked as continuous lines of moderate to high variance coefficients radiating from the vents on the variance time slices (Figures 12 to 16). Radial faults in the study area have variable strike and are predominant at depths of approximately 1800 to 3000 ms, where they show a distinctive orientation that contrasts with those of tectonic and polygonal faults (Figures 3, 4a, 12 to 16). Large tectonic faults in the study area can reach approximately 40 km in length and are oriented dominantly in an E-W direction, while the smaller tectonic faults (less than 10 km in length) are oriented in N-S, NW-SE and NE-SW directions (Figures 4b, See Omosanya et al., 2017). The polygonal faults in the study area on the other hand have polygonal planform and in profile are developed in tiers across the Upper Tang Formation to the Brygge Formation. The closely spaced or upper tier polygonal faults are predominant within the Eocene to Early Miocene Brygge Formation, i.e., the H8-H7 strata (Figure 4). Polygonal faults are widespread within the Cenozoic succession of the Vøring Basin (Gay and Berndt, 2007; Laurent et al., 2012).

A significant observation from a first-look interpretation of the radial faults from the time slices is their distinct variability across different depths (Figures 12 to 16). In addition, vent-radial faults have different types of faults associated with their conduits at deeper depths, suggesting that the overlying radial faults are possibly dip-linked with the other fault types at depth (e.g., Figure 13). Consequently, five representative vents with associated radial faults have been selected to demonstrate the differences in the character of the radial faults in the study area. These are V2, V6, V7, V11 and V15 (Figure 12 to 16). Here, fifty-three (53) radial faults have been interpreted across these five vents. An important outcome of these interpretations is that radial faults on the vents' summits show close tip and cross cutting interactions with polygonal faults. These types of radial faults are restricted to shallow stratigraphic levels and are presumably linked to other fault types at depth. Faults at this deeper depth intersect the vents' conduits and are located below the overlying hydrothermal vents. For example, V2 has radial faults that are common between 2250 to 2700 ms (Figures 12a to 12d). Eight of these radial faults on V2 strike in NE, SW, and E-W directions, with dips to the W, NW and NNE (Figure 12c). At depths below 2700 ms, the radial faults disappear, with polygonal faults becoming more prominent and interacting with the vent conduit (Figures 12e and 12f).

Furthermore, V6 shows a marked transition from radial faulting at its zenith to more aligned faults at depth (Figure 13). These radial faults occur between depths of 1950 to 2250 ms TWTT above the summit of V6 and strike in NE-SW and NW-SE directions, with dips to the NE, N, S and NW (Figure 13a). At a depth of approximately 2500 ms, the fault types around the conduit of V6 change to

concentric fault type (Figure 13b), which in turn become well-aligned NW-SE faults at depths of 3000 ms and beyond (Figure 13c). Faults interpreted at the summit of V7 radiate in almost all directions, with dip directions dominantly to the north (Figures 5a and 14). An important character of these radial faults at the summit of V7 is that they are delimited by polygonal faults from the top to base (Figures 14a and 14c). Furthermore, the radial faults associated with the summit of V11 occur from depths of 1900 to 2200 ms (Figure 15). However, at depths beyond 2200 ms TWTT, the conduit of V11 is associated with polygonal faults and faults oriented in NW-SE and NE-SW directions (Figure 15e).

An exceptional cross-sectional view of radial faults-conduit interaction is presented in Figure 15. On seismic sections, antithetic normal faults dipping towards each other intersect the conduit of V15. However, the interpretation of the faults on the variance slice shows that the radial faults inundating the summit of V15 have conspicuous a radiating pattern (Figures 16c and 16d). By contrast, at depths of 2500 ms TWTT and beyond, the large antithetic normal faults are seen to be part of a network of polygonal faults rather than radial faults (Figure 16e), which is an indication that the observed geometry in cross section is probably due to the reorganization of the fault orientation during vent formation. In parallel, the majority of vent conduits show no evidence of associated radial faults. Instead, most of the vent conduits are intersected by large tectonic normal faults and, in a few cases, by polygonal faults (e.g., Figures 4b, 6d, 15a and 15e).

6. Discussion

6.1 Origin and character of hydrothermal vents

The origin of the hydrothermal vent complexes in this study is inferred from seismic facies analyses, which suggest that subsurface plumbing of hydrothermal fluids from the underlying magmatic sill complexes is the main mechanism for their formation (Planke et al., 2005; Hansen, 2006). Distinctive seismic facies of the hydrothermal vent complexes when compared to those of their host-rock succession are (a) chaotic pyramidal, conical to cylindrical low amplitude conduits, (b) dome- and eye-shaped upper parts, (c) intermediate dipping reflections, (d) radial faults at the vents' summit and (e) preferred locations of the base of the vents' conduits at the tips of the underlying magmatic sills.

The presence of these seismic characteristics suggest that magmatic intrusions probably mobilized fluids and led to piercing of the overburden strata. For the hydrothermal vent complexes to form through such a process, the local fluid pressure must be larger than the hydrostatic pressure (Jamtveit et al., 2004). This overpressure build-up can only occur if the pressure build-up is faster than the pressure release, i.e., the host-rock permeability is small, and the pressure generation is fast (Jamtveit et al. 2004). Pressure increases from the sills would lead to boiling of the host-rock, degassing of the intruded magma and fracturing of the overburden (Judd and Hovland, 2007; Planke et al., 2005). Alternatively, fluid overpressure may be generated during metamorphic dehydration reactions when

various gases such as CO₂, SO₂ and halocarbons are released (Aarnes et al., 2010). Generation of large quantities of gaseous hydrocarbons such as CH₄ could result in large overpressures that trigger catastrophic blowouts and the formation of hydrothermal vent complexes (Aarnes et al., 2012; Iyer et al., 2017). The vertical zones described here are as hydrothermal conduits; with the chaotic to low amplitude reflections signify such blow out structures, the passage of fluids and infill of ejected materials such as sediment breccia and sand through the conduits (Heggland, 1998; Jamtveit et al., 2004; Planke et al., 2005; Svensen et al., 2006). Accordingly, the morphology of the vents' summits, forming eyes or domes together with the presence of internal dipping reflections, are further pointers to a vent-induced process (Hansen, 2006; Planke et al., 2005). Craters at the upper parts of hydrothermal vents are usually infilled by ejected material to form vents with eye-shaped upper parts, while domes at the vents' crests are formed when the expulsion is less energetic and craters do not form (Planke et al., 2005).

Understanding sill emplacement mechanisms and timing is important for unravelling the genesis and geometries of the vents studied in this work. Sills underlying the vents show a progressive development that is suggestive of incremental sill emplacement. The presence of several sills at disparate stratigraphic intervals evidence a protracted sill emplacement time from the melt source (Magee et al., 2014; Magee et al., 2016). Under such circumstances, the magma migration pathway must remain operational over time; such that the magma feeding the sills would have prolonged residence times and new magma pulses are intruded into environments of relatively high temperature (Annen, 2011; Broderick et al., 2015). The maintenance of locally elevated temperatures might have allowed later magma pulses to remain hotter for longer times and further facilitate intrusion up into the stratigraphic sequence (Magee et al., 2016). As for the timing of sill intrusions, we propose an Early Eocene timing of magmatic emplacement based on the occurrence of seismic-stratigraphic markers such as onlap reflections on the folds in Figures 2a, 6c and 7. Onlap reflections indicate that fold growth was generated by and accommodated sill emplacement, resulting in the formation of bathymetric highs that were onlapped by syn-kinematic sediments (Hansen and Cartwright, 2006; Jackson et al., 2013). The onlapping sediments are part of the Mid Eocene-Miocene Brygge Formation, while the majority of vents are within the Palaeocene to Eocene H7-H8 strata (Figure 2a). As a result, sill emplacement in the study area is linked to breakup magmatism in the Early Eocene during the opening of the Norwegian-Greenland Seas. This timing further corroborates previous dates of magmatic emplacement in the study area and in the Vøring Basin (Hansen, 2006; Omosanya et al., 2017; Planke et al., 2005; Svensen et al., 2010; Svensen et al., 2004).

Consequently, we provide relative dating of the vents based on the positioning or terminations of the vents within the host-rock strata. The majority of the vents are located within the Eocene to Oligocene H7-H8 strata, while others are interpreted within the H8-H9 strata and marginally at the H6-

H5 level (Figures 5a to 5c). The first two occurrences provide evidence for Eocene venting in tandem with Eocene magmatic emplacement in the study area. However, the upper terminations of the vents may not necessarily define the time of vent formation but rather indicate fluid dissipation into a subsurface reservoir (Hustoft et al., 2009). Nonetheless, the deposition of the H7-H9 strata predates the vents and as such signifies an Eocene to Oligocene timing of vent formation in the study area. An additional phase of vent formation is probably indicated by vents' termini observed at the H6 level (e.g., V4, Figure 5d), which is an Oligocene and Miocene Formation, hinting at the possibility of vent formation occurring within hundreds of years after the emplacement of magmatic sills (Hansen, 2006; Iyer et al., 2013).

Regarding the geometries of the observed hydrothermal conduits, the conical- and cylindrical - shaped conduits as observed from this study importantly confirms the shape of archetypal hydrothermal vent conduits as described by Planke et al. (2005) and Svensen et al. (2006). In which the authors favoured hydrothermal vent complexes that usually become wider from base to top (Figure 17a). In this study, we have identified hydrothermal vent conduits with similar geometries but notably also found conduits with a geometry deviating from those previously established. We hypothesize that the geometry of the pyramid-shaped conduits observed in this work reflects the influence of vertical stack of sills associated with them and likely provide an explanation for the irregular variation in their widths especially at intermediate levels (Figure 7). Thus, pyramid-shaped conduits may manifest the modification of pre-existing conduits by fluids associated with incremental sill emplacement (Figure 17b).

6.2 Relationship between radial faults and hydrothermal vents

Radial faults associated with the vents' summits in the study area have different trends compared to the tectonic faults, signifying that they probably formed by independent mechanisms and are mutually exclusive. The latter assertion is supported by (a) the general restriction of the radial faults to the vents' summits and (b) changes in fault types associated with the vents' conduits from top to base (Figures 4b, 12- 16). As regards polygonal faults and their interaction with the radial faults, the upper tier polygonal faults are the ones bounding most of the radial faults in Figures 12 to 16. First, we reiterate that the polygonal faults span the Palaeocene Tang Formation to the Eocene/Early Miocene Brygge Formation, suggesting the possibility that some of the polygonal faults formed prior to magmatic emplacement and vent formation in the study area (see Omosanya et al., 2017). Based on this notion and the occurrence of radial faults with both dome- and eye-shaped types (Figures 12-16, Table 1), we

provide two likely mechanisms for the formation of the vent-related radial faults below (Figures 17b and 17c).

In the first instance where radial faults are found on the crests of both eye-shaped and dome-shaped vents, we hypothesize that the radial faults formed due to the extension of the overburden during fluid dissipation (Figure 17b). Thus, the overburden is arched or domed, and the radial faults developed to accommodate the outer-arc and circumferential extension of the palaeo seafloor (Hansen and Cartwright, 2006). This is plausible as the domes' growths must be accommodated by penetrative strain, which is expressed as radial faults in zones that are sufficiently compacted to show brittle failure at the scale of seismic resolution (Goult, 2008; Lisle, 1994). Domes at the tops of some of the vents provided additional insights into the role of differential compaction during hydrothermal vent formation. Differential compaction is common in inhomogeneous sedimentary deposits where material rheology varies (Miles and Cartwright, 2010; Xu et al., 2015). Domes or folds at the top of the vents would have formed due to differential compaction as these structures were buried and the surrounding strata compact more than the vents themselves (Skogseid et al., 1992; Planke et al., 2005). Increased compaction at the sides of the vents means that the strata on top have to fold across the vent (Figure 17b). These are differential compaction folds and are ubiquitous in many sedimentary basins (Zhao et al., 2014). Hence, the radial faults developed above or intersected such compaction folds and are formed when the overburden is arched (e.g., V21, Figure 6c). This mechanism is analogous to radial faults formed on salt diapirs (Davison et al., 2000; Stewart, 2006). In a manner similar to salt-related radial faults, the limit of doming of the vents is dependent on the magnitude of the stresses during venting, with hoop stresses restricted to the vents' width (Moreau et al., 2012; Stewart, 2006).

The above model is inadequate to explain the occurrence of radial faults associated with craters or the bases of eye-shaped vents such as V11, V15 and V18. On the other hand, we considered the influence of fluid venting on the modification of polygonal fault systems and regional/basin stress field (Figure 17c). Polygonal fault systems usually form by contraction-driven shear failure during the early stages of sediment compaction and dewatering in subsiding sedimentary basins, which are free of lateral tectonic forces (Goult, 2001). The maximum compressive stress (S_v) is vertical, while the intermediate (S_H) and least compressive stresses (S_h) are horizontal during one-dimensional consolidation of the sediment layer (Terzaghi et al., 1996). Horizontal stress is thus effectively isotropic in basins where polygonal faults form, highlighting their diversity and lack of preferred orientations (Cartwright, 2011; Dewhurst et al., 1999; Goult, 2001; Lonergan et al., 1998). Local perturbations of the regional stress regime within polygonal faults systems due to diapirism and fluid venting can cause part of the polygonal faults to realign, forming radial faults in such a manner that maximum compressive stress is radial and the minimum stress is circumferential, overriding the regional stress field (Carruthers et al., 2013). Similar mechanisms have been proposed for radial faults developed around pockmark craters,

salt withdrawal basins, salt stocks and salt walls in the Espírito Santo Basin and Central North Sea (e.g., Carruthers et al., 2013). Radial faults formed in such settings are layer-bounded in the same discrete layer as the polygonal fault systems and are classified as perturbed members of the basin-wide polygonal fault system. These types of radial faults propagate primarily under the influence of compaction and contraction but in an anisotropic stress field. Based on the preceding information, we propose that the radial faults associated with the eye-/crater-shaped vent (e.g., V2, Figure 12) formed as part of a spatially related polygonal fault network. Local perturbation of the stress regime within the polygonal fault systems due to intrusion-related focused fluid-flow, which was enhanced by differential compaction of the palaeoseafloor led to the realignment of polygonal faults adjacent to the hydrothermal vents in a radial pattern. However, other interpretations in the context of the regional and local stress regimes might also be applicable.

6.3 Seismic resolution of the interpreted magmatic sills, hydrothermal vent complexes and radial faults.

After discussing the origin and mechanisms behind the formation of the magmatic sills, hydrothermal vent complexes and radial faults in the study area. It is important to emphasize the accuracy and caveats inherent in their interpretations. The magmatic sills, hydrothermal vent complexes and radial faults interpreted here suffer the same setback as most seismic features in that they are not actually drilled. Hence, it is impossible to authenticate their true nature and lithology. Specifically, magmatic sills in this study are tuned reflections with tops and bases that cannot be distinguished (Brown, 2004; Smallwood and Maresh, 2002). This is because the sills have vertical thicknesses that lie between the limit of vertical resolution, i.e., $\lambda/4$ and the limit of detectability, i.e., $\lambda/32$ (Sheriff and Geldart, 1999; Yilmaz, 2001). Tuning introduces uncertainty in the interpretation, making it difficult to separate real features from geophysical artefacts (Smallwood and Maresh, 2002).

In addition to those lost due to the vertical resolution, a number of other sills could have been omitted during the interpretation simply because their seismic imaging is also dependent on a number of other factors. These include the frequency of the data, inadequate velocity models, sill thickness, overburden complexity, interference between the reflections from closely spaced sills, and the style of the host rock (Brown 2004; Magee et al., 2015; Eide et al., 2017). For example, overlying sills could screen and affect the imaging of sills and rocks underneath by decreasing seismic amplitude, frequency and making steeply dipping features almost impossible to image (Eide et al., 2017; Lecomte et al., 2015). This is particularly applicable considering that dykes are not identified in the study area. It is not impossible that vertical intrusions or dykes facilitated sill migration in the study area. However, dikes and other vertical structures are hardly imaged on seismic data because of the low amount of acoustic energy that reflects back to the surface from them (Thomson, 2007).

The seismic imaging of the hydrothermal conduits is largely dependent on lateral resolution and its internal structures (Brown, 2004; Cartwright and Santamarina, 2015; Kjoberg et al., 2017). The internal configuration of the vent conduits cannot be imaged when they have a diameter that is of the order of the lateral resolution limit (Brown, 2004). Additionally, accuracy in the imaging is less certain with increasing depth down the conduits and with decreasing conduit' width, while the identification of the lateral margins of the conduits is affected by data/imaging quality (Løseth et al., 2011; Yilmaz, 2001). Accordingly, the synthetic models of Kjoberg et al. (2017) in the Møre Basin show that the imaging of conduit structures is dependent on the dips of the surrounding strata. These authors conclude that processed seismic data are likely unable to visualize surrounding host-rock strata or reflections with dip angles exceeding 45° . Importantly, the presence of 'acoustic blanking zones' beneath the sills might have influenced the observed pyramid-shaped conduits, especially when these ABZs are vertically stacked, thus, masking the seismic imaging of weaker sills and reflections beneath (e.g., Figures 7b and 9b). This is particularly relevant considering that sill complexes exhibit large lateral variations in effective velocity in the subsurface (Eide et al., 2017). As a corollary, migration artefacts caused by this lateral variation in the effective velocity of sills are capable of masking weak reflections or stratigraphy (Gray et al., 2001).

As for the interpreted radial faults, a common caveat inherent during their interpretation is related to the over reliance on seismic attribute maps for fault mapping. This is especially common and applicable to amplitude, time dip and coherence (variance) maps, which are generally bedevilled with linear structures that are often mistaken as faults (Hesthammer et al., 2001; Marfurt and Alves, 2015). As a result, a cautious use of the variance time slices for radial fault mapping in this work was undertaken. Particularly, the faults and vents that were interpreted on the slices were ground truth on seismic profiles to ascertain that they are truly discontinuities and structures and not seismic artefacts.

7. Conclusions

Hydrothermal vent complexes in the study area formed due to the release of fluids from the underlying sill complexes, which were emplaced during the continental breakup and opening of the Norwegian and Greenland Seas in the Early Eocene. The magmatic sills in the study area show a remarkable positive amplitude character, complex seismic stratigraphic behaviour and association with distinctive seismic facies. Fluids released from the magmatic sills ascended into the lower stratigraphic layers, creating remarkable seismic signatures, which include dipping reflectors, radial faults, domes and craters at the summits of vents. Radial faults represent outstanding seismic features that mark local perturbations of either the overburden or regional stress regime within a polygonal fault system by fluid venting in the study area. Radial faulting induced by hydrothermal fluid circulation is formed in response to extension of the overburden and is similar to that previously described from salt-rich margins. We identify three end-member conduits that connect the hydrothermal vents to their source

sills. These include pyramid-, conical- and cylindrical-shaped conduits. A statistical criterion of importance that is used to distinguish conduits is their width 'w' within the host-rock succession. Pyramid-shaped conduits have an increasing 'w' with depth, conical-shaped conduits have an inverse trend of 'w' with depth, and cylindrical-shaped conduits have an almost constant 'w' with depth. We conclude that the architecture of pyramid-shaped conduits is modified either because of incremental sill emplacement or due to problems of seismic imaging of weaker reflections beneath vertically stacked sills.

Acknowledgements

Kamal acknowledges provision of data from IGP-NTNU and the Norwegian Petroleum Directorate. The authors also recognize the Norwegian Petroleum Directorate (NPD) for graciously granting access to the borehole data used in this research and Schlumberger for provision of Petrel® and Petrel ready project for seismic interpretation. Ovie Emmanuel Eruteya is grateful to the Graduate Studies Authority of University of Haifa for funding his doctoral research. We are deeply grateful to David Lacopini, Stefan Bünz and an anonymous reviewer for their suggestions and reviews that greatly improved the outlook of the manuscript. We also thank Craig Magee and Julien Moreau for their comments and insightful suggestions on the initial draft of the manuscript.

References

- Aarnes, I., Planke, S., Trulsvik, M., Svensen, H., 2015. Contact metamorphism and thermogenic gas generation in the Vøring and Møre basins, offshore Norway, during the Paleocene–Eocene thermal maximum. *Journal of the Geological Society* 172, 588-598.
- Aarnes, I., Podladchikov, Y., Svensen, H., 2012. Devolatilization-induced pressure build-up: Implications for reaction front movement and breccia pipe formation. *Geofluids* 12, 265-279.
- Aarnes, I., Svensen, H., Connolly, J.A., Podladchikov, Y.Y., 2010. How contact metamorphism can trigger global climate changes: Modeling gas generation around igneous sills in sedimentary basins. *Geochimica et Cosmochimica Acta* 74, 7179-7195.
- Alsop, G.I., 1996. Physical modelling of fold and fracture geometries associated with salt diapirism. Geological Society, London, Special Publications 100, 227-241.
- Alves, T.M., Omosanya, K.O., Gowling, P., 2015. Volume rendering of enigmatic high-amplitude anomalies in southeast Brazil: A workflow to distinguish lithologic features from fluid accumulations. *Interpretation* 3, 1-14.
- Annen, C., 2011. Implications of incremental emplacement of magma bodies for magma differentiation, thermal aureole dimensions and plutonism–volcanism relationships. *Tectonophysics* 500, 3-10.
- Brekke, H., 2000. The tectonic evolution of the Norwegian Sea Continental Margin with emphasis on the Voring and More Basins. Geological Society, London, Special Publications 167, 327-378.
- Broderick, C., Wotzlaw, J.F., Frick, D., Gerdes, A., Ulianov, A., Günther, D., Schaltegger, U., 2015. Linking the thermal evolution and emplacement history of an upper-crustal pluton to its lower-crustal roots using zircon geochronology and geochemistry (southern Adamello batholith, N. Italy). *Contributions to Mineralogy and Petrology* 170, 28.
- Brown, A., 2004. Interpretation of three-dimensional seismic data: The American Association of Petroleum Geologists and the Society of Exploration Geophysicists. Tulsa, OK 535.
- Bukovics, C., Ziegler, P.A., 1985. Tectonic development of the Mid-Norway continental margin. *Marine and Petroleum Geology* 2, 2-22.

- Carruthers, D., Cartwright, J., Jackson, M.P., Schutjens, P., 2013. Origin and timing of layer-bound radial faulting around North Sea salt stocks: New insights into the evolving stress state around rising diapirs. *Marine and Petroleum Geology* 48, 130-148.
- Cartwright, J., 2011. Diagenetically induced shear failure of fine-grained sediments and the development of polygonal fault systems. *Marine and Petroleum Geology* 28, 1593-1610.
- Cartwright, J., Santamarina, C., 2015. Seismic characteristics of fluid escape pipes in sedimentary basins: implications for pipe genesis. *Marine and Petroleum Geology* 65, 126-140.
- Dalland, a., Worsley, D., Ofstad, K., 1988. A lithostratigraphic scheme for the Mesozoic and Cenozoic succession offshore mid- and northern Norway, Norwegian Petroleum Directorate Bulletin, p. 65.
- Davison, I., Alsop, I., Birch, P., Elders, C., Evans, N., Nicholson, H., Rorison, P., Wade, D., Woodward, J., Young, M., 2000. Geometry and late-stage structural evolution of Central Graben salt diapirs, North Sea. *Marine and Petroleum Geology* 17, 499-522.
- Deegan, C., Scull, B.J., 1977. A standard lithostratigraphic nomenclature for the Central and Northern North Sea. HMSO.
- Dewhurst, D.N., Cartwright, J.A., Lonergan, L., 1999. The development of polygonal fault systems by syneresis of colloidal sediments. *Marine and Petroleum Geology* 16, 793-810.
- Doré, A., Lundin, E., Fichler, C., Olesen, O., 1997. Patterns of basement structure and reactivation along the NE Atlantic margin. *Journal of the Geological Society* 154, 85-92.
- Doré, A.G., Lundin, E.R., Jensen, L.N., Birkeland, Ø., Eliassen, P.E., Fichler, C., 1999. Principal tectonic events in the evolution of the northwest European Atlantic margin, Geological society, london, petroleum geology conference series. Geological Society of London, pp. 41-61.
- Eide, C.H., Schofield, N., Lecomte, I., Buckley, S.J., Howell, J.A., 2017. Seismic interpretation of sill complexes in sedimentary basins: implications for the sub-sill imaging problem. *Journal of the Geological Society*, jgs2017-2096.
- Eidvin, T., Brekke, H., Riis, F., Renshaw, D.K., 1998. Cenozoic stratigraphy of the Norwegian Sea continental shelf 64degreesN-68degreesN. *Norsk Geologisk Tidsskrift* 78, 125-151.
- Eidvin, T., Riis, F., Rasmussen, E., Rundberg, Y., 2013. Investigation of Oligocene to Lower Pliocene deposits in the Nordic offshore area and onshore Denmark. *NPD Bulletin* 10, 62.
- Eldholm, O., Thiede, J., Taylor, E., 1989. Evolution of the Vøring Volcanic Margin, Proceedings of the Ocean Drilling Program, 104 Scientific Results, pp. 1033-1065.
- Gay, A., Berndt, C., 2007. Cessation/reactivation of polygonal faulting and effects on fluid flow in the Vøring Basin, Norwegian Margin. *Journal of the Geological Society* 164, 129-141.
- Goult, N., 2001. Mechanics of layer-bound polygonal faulting in fine-grained sediments. *Journal of the Geological Society* 159, 239-246.
- Goult, N., 2008. Geomechanics of polygonal fault systems: a review. *Petroleum Geoscience* 14, 389-397.
- Gray, S.H., Etgen, J., Dellinger, J., Whitmore, D., 2001. Seismic migration problems and solutions. *Geophysics* 66, 1622-1640.
- Grove, C., 2013. Submarine hydrothermal vent complexes in the Paleocene of the Faroe-Shetland Basin: Insights from three-dimensional seismic and petrographical data. *Geology* 41, 71-74.
- Hansen, D., Cartwright, J., 2003. The geometry and emplacement of igneous sills in volcanic margins: The role of faulting, EGS-AGU-EUG Joint Assembly.
- Hansen, D.M., 2006. The morphology of intrusion-related vent structures and their implications for constraining the timing of intrusive events along the NE Atlantic margin. *Journal of the Geological Society* 163, 789-800.
- Hansen, D.M., Cartwright, J., 2006. The three-dimensional geometry and growth of forced folds above saucer-shaped igneous sills. *Journal of Structural Geology* 28, 1520-1535.
- Hegglund, R., 1998. Gas seepage as an indicator of deeper prospective reservoirs. A study based on exploration 3D seismic data. *Marine and Petroleum Geology* 15, 1-9.
- Hesthammer, J., Landrø, M., Fossen, H., 2001. Use and abuse of seismic data in reservoir characterisation. *Marine and Petroleum Geology* 18, 635-655.
- Hustoft, S., Bünz, S., Mienert, J., Chand, S., 2009. Gas hydrate reservoir and active methane-venting province in sediments on < 20 Ma young oceanic crust in the Fram Strait, offshore NW-Svalbard. *Earth and Planetary Science Letters* 284, 12-24.

- Iyer, K., Rüpke, L., Galerne, C.Y., 2013. Modeling fluid flow in sedimentary basins with sill intrusions: Implications for hydrothermal venting and climate change. *Geochemistry, Geophysics, Geosystems* 14, 5244-5262.
- Iyer, K., Schmid, D.W., Planke, S., Millett, J., 2017. Modelling hydrothermal venting in volcanic sedimentary basins: Impact on hydrocarbon maturation and paleoclimate. *Earth and Planetary Science Letters* 467, 30-42.
- Jackson, C.A.L., Schofield, N., Golenkov, B., 2013. Geometry and controls on the development of igneous sill-related forced folds: A 2-D seismic reflection case study from offshore southern Australia. *Geological Society of America Bulletin* 125, 1874-1890.
- Jamtveit, B., Svensen, H., Podladchikov, Y.Y., Planke, S., 2004. Hydrothermal vent complexes associated with sill intrusions in sedimentary basins. Geological Society, London, Special Publications 234, 233-241.
- Judd, A., Hovland, M., 2007. *Seabed Fluid Flow: The Impact on Geology, Biology and the Marine Environment*. Cambridge University Press, Cambridge.
- Kjoberg, S., Schmiedel, T., Planke, S., Svensen, H.H., Millett, J.M., Jerram, D.A., Galland, O., Lecomte, I., Schofield, N., Haug, Ø.T., 2017. 3D structure and formation of hydrothermal vent complexes at the Paleocene-Eocene transition, the Møre Basin, mid-Norwegian margin. *Interpretation* 5, SK65-SK81.
- Laurent, D., Gay, A., Baudon, C., Berndt, C., Soliva, R., Planke, S., Mourgues, R., Lacaze, S., Pauget, F., Mangué, M., Lopez, M., 2012. High-resolution architecture of a polygonal fault interval inferred from geomodel applied to 3D seismic data from the Gjallar Ridge, Vøring Basin, Offshore Norway. *Marine Geology* 332-334, 134-151.
- Lecomte, I., Lavadera, P.L., Anell, I., Buckley, S.J., Schmid, D.W., Heeremans, M., 2015. Ray-based seismic modeling of geologic models: Understanding and analyzing seismic images efficiently. *Interpretation* 3, SAC71-SAC89.
- Lisle, R.J., 1994. Detection of zones of abnormal strains in structures using Gaussian curvature analysis. *AAPG Bulletin* 78, 1811-1819.
- Lonergan, L., Cartwright, J., Jolly, R., 1998. The geometry of polygonal fault systems in Tertiary mudrocks of the North Sea. *Journal of Structural Geology* 20, 529-548.
- Lundin, E., Doré, A.G., 2002. Mid-Cenozoic post-breakup deformation in the 'passive' margins bordering the Norwegian-Greenland Sea. *Marine and Petroleum Geology* 19, 79-93.
- Løseth, H., Wensaas, L., Gading, M., Duffaut, K., Springer, M., 2011. Can hydrocarbon source rocks be identified on seismic data? *Geology* 39, 1167-1170.
- Magee, C., Jackson, C.A.L., Schofield, N., 2014. Diachronous sub-volcanic intrusion along deep-water margins: insights from the Irish Rockall Basin. *Basin Research* 26, 85-105.
- Magee, C., Maharaj, S.M., Wrona, T., Jackson, C.A.L., 2015. Controls on the expression of igneous intrusions in seismic reflection data. *Geosphere* 11, 1024-1041.
- Magee, C., Muirhead, J.D., Karvelas, A., Holford, S.P., Jackson, C.A.L., Bastow, I.D., Schofield, N., Stevenson, C.T.E., McLean, C., McCarthy, W., 2016. Lateral magma flow in mafic sill complexes. *Geosphere* 12, 809-841.
- Mansfield, C., Cartwright, J., 1996. High resolution fault displacement mapping from three-dimensional seismic data: evidence for dip linkage during fault growth. *Journal of Structural Geology* 18, 249-263.
- Marfo, G., Omosanya, O.K., Johansen, E.S., Abrahamson, P., 2017. Seismic interpretation and characterization of anhydrite caprocks in the Tromsø Basin, SW Barents Sea. *Marine Geology* 390, 36-50.
- Marfurt, K., Alves, T., 2015. Pitfalls and limitations in seismic attribute interpretation of tectonic features: *Interpretation*, 3, SB5-SB15.
- Mattos, N.H., Alves, T.M., Omosanya, K.O., 2016. Crestal fault geometries reveal late halokinesis and collapse of the Samson Dome, Northern Norway: Implications for petroleum systems in the Barents Sea. *Tectonophysics* 690, 76-96.
- Mazzini, A., Svensen, H., Hovland, M., Planke, S., 2006. Comparison and implications from strikingly different authigenic carbonates in a Nyegga complex pockmark, G11, Norwegian Sea. *Marine Geology* 231, 89-102.

- Miles, A., Cartwright, J., 2010. Hybrid flow sills: A new mode of igneous sheet intrusion. *Geology* 38, 343-346.
- Mohammedyasin, S.M., Lippard, S.J., Omosanya, K.O., Johansen, S.E., Harishidayat, D., 2016. Deep-seated faults and hydrocarbon leakage in the Snøhvit Gas Field, Hammerfest Basin, Southwestern Barents Sea. *Marine and Petroleum Geology* 77, 160-178.
- Moreau, J., Ghienne, J.F., Hurst, A., 2012. Kilometre-scale sand injectites in the intracratonic Murzuq Basin (South-west Libya): an igneous trigger? *Sedimentology* 59, 1321-1344.
- Muirhead, J.D., Airoidi, G., White, J.D., Rowland, J.V., 2014. Cracking the lid: Sill-fed dikes are the likely feeders of flood basalt eruptions. *Earth and Planetary Science Letters* 406, 187-197.
- Ngeri, A., Tamunobereton-ari, I., Amakiri, A., 2015. Ant-tracker attributes: an effective approach to enhancing fault identification and interpretation. *Journal of VLSI and Signal Processing* 5, 67-73.
- Omosanya, K.O., Johansen, S.E., Abrahamson, P., 2016. Magmatic activity during the breakup of Greenland-Eurasia and fluid-flow in Stappen High, SW Barents Sea. *Marine and Petroleum Geology* 76, 397-411.
- Omosanya, K.O., Johansen, S.E., Eruteya, O.E., Waldmann, N., 2017. Forced folding and complex overburden deformation associated with magmatic intrusion in the Vøring Basin, offshore Norway. *Tectonophysics* 706-707, 14-34.
- Ostendorf, P., Gundersen, A., 2003. AVO Quick Look Visualization Technique, Naglfar Dome, Norwegian Sea, 65th EAGE Conference & Exhibition.
- Planke, S., Rasmussen, T., Rey, S.S., Myklebust, R., 2005. Seismic characteristics and distribution of volcanic intrusions and hydrothermal vent complexes in the Vøring and Møre basins. *Petroleum Geology: North-West Europe and Global Perspectives* 6, 833-844.
- Pollard, D.D., Muller, O.H., Dockstader, D.R., 1975. The form and growth of fingered sheet intrusions. *Bulletin of the Geological Society of America* 86, 351-363.
- Reynolds, P., Planke, S., Millett, J.M., Jerram, D.A., Trulsvik, M., Schofield, N., Myklebust, R., 2017. Hydrothermal vent complexes offshore Northeast Greenland: A potential role in driving the PETM. *Earth and Planetary Science Letters* 467, 72-78.
- Schofield, N., Brown, D.J., Magee, C., Stevenson, C.T., 2012. Sill morphology and comparison of brittle and non-brittle emplacement mechanisms. *Journal of Structural Geology* 169, 127-141.
- Sheriff, R.E., Geldart, L.P., 1999. *Exploration seismology*. Univ. Press, Cambridge.
- Skogseid, J., Pedersen, T., Eldholm, O., Larsen, B.T., 1992. Tectonism and magmatism during NE Atlantic continental break-up: the Vøring basin. *Magmatism and the Causes of Continental Break-up* 68, 305-320.
- Smallwood, J.R., Maresh, J., 2002. The properties, morphology and distribution of igneous sills: modelling, borehole data and 3D seismic from the Faroe-Shetland area. *Geological Society, London, Special Publications* 197, 271-306.
- Stewart, S.A., 2006. Implications of passive salt diapir kinematics for reservoir segmentation by radial and concentric faults. *Marine and Petroleum Geology* 23, 843-853.
- Svensen, H., Jamtveit, B., Planke, S., Chevallier, L., 2006. Structure and evolution of hydrothermal vent complexes in the Karoo Basin, South Africa. *Journal of the Geological Society* 163, 671-682.
- Svensen, H., Planke, S., Chevallier, L., Malthe-Sørenssen, A., Corfu, F., Jamtveit, B., 2007. Hydrothermal venting of greenhouse gases triggering Early Jurassic global warming. *Earth and Planetary Science Letters* 256, 554-566.
- Svensen, H., Planke, S., Corfu, F., 2010. Zircon dating ties NE Atlantic sill emplacement to initial Eocene global warming. *Journal of the Geological Society* 167, 433-436.
- Svensen, H., Planke, S., Jamtveit, B., Pedersen, T., 2003. Seep carbonate formation controlled by hydrothermal vent complexes: A case study from the Vøring Basin, the Norwegian Sea. *Geo-Marine Letters* 23, 351-358.
- Svensen, H., Planke, S., Malthe-Sørenssen, A., Jamtveit, B., Myklebust, R., Eidem, T.R., Rey, S.S., 2004. Release of methane from a volcanic basin as a mechanism for initial Eocene global warming. *Nature* 429, 542.
- Terzaghi, K., Peck, R.B., Mesri, G., 1996. *Soil mechanics in engineering practice*. John Wiley & Sons.

- Thomson, K., 2007. Determining magma flow in sills, dykes and laccoliths and their implications for sill emplacement mechanisms. *Bulletin of Volcanology* 70, 183-201.
- Thomson, K., Hutton, D., 2004. Geometry and growth of sill complexes: Insights using 3D seismic from the North Rockall Trough. *Bulletin of Volcanology* 66, 364-375.
- Walker, R., Healy, D., Kawanzaruwa, T., Wright, K., England, R., McCaffrey, K., Bubeck, A., Stephens, T., Farrell, N., Blenkinsop, T., 2017. Igneous sills as a record of horizontal shortening: The San Rafael subvolcanic field, Utah. *GSA Bulletin* 129, 1052-1070.
- Withjack, M.O., Scheiner, C., 1982. Fault patterns associated with domes--an experimental and analytical study. *AAPG Bulletin* 66, 302-316.
- Xu, S., Hao, F., Xu, C., Wang, Y., Zou, H., Gong, C., 2015. Differential compaction faults and their implications for fluid expulsion in the northern Bozhong Subbasin, Bohai Bay Basin, China. *Marine and Petroleum Geology* 63, 1-16.
- Yilmaz, Ö., 2001. *Seismic data analysis*. Society of Exploration Geophysicists.
- Yin, H., Groshong Jr, R.H., 2003. Geometric properties of active piercement structures: geologic insights from 3-D kinematic models.
- Zervas, I., Omosanya, K., Lippard, S., Johansen, S., 2018. Fault kinematics and localised inversion within the Troms-Finnmark Fault Complex, SW Barents Sea. *Journal of Structural Geology*.
- Zhao, F., Wu, S., Sun, Q., Huuse, M., Li, W., Wang, Z., 2014. Submarine volcanic mounds in the Pearl River mouth basin, northern South China Sea. *Marine Geology* 355, 162-172.

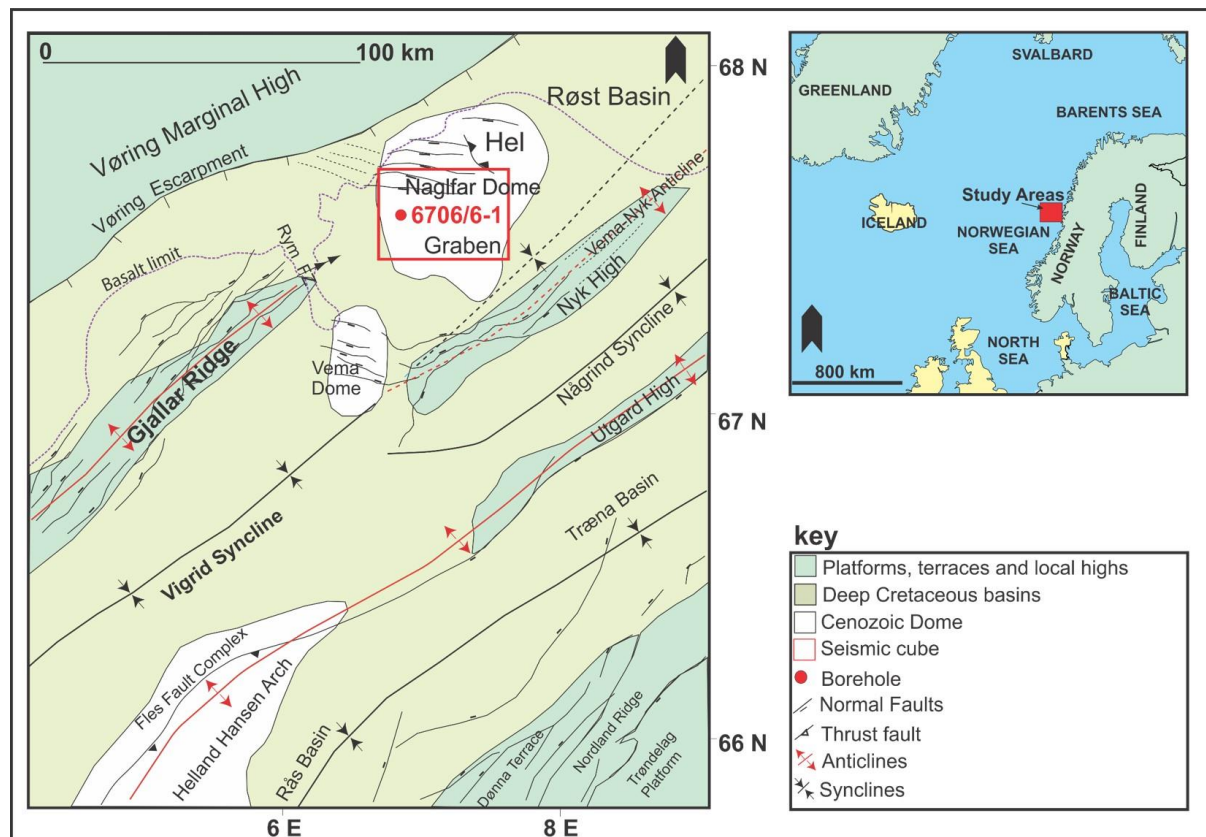


Figure 1: Location of the study area in the context of the Vøring Basin. The seismic survey for the study is shown in the red rectangle, while the red dot corresponds to the position of the borehole used for the seismic-well tie and lithostratigraphic description. The map is modified after Lundin et al. (2013).

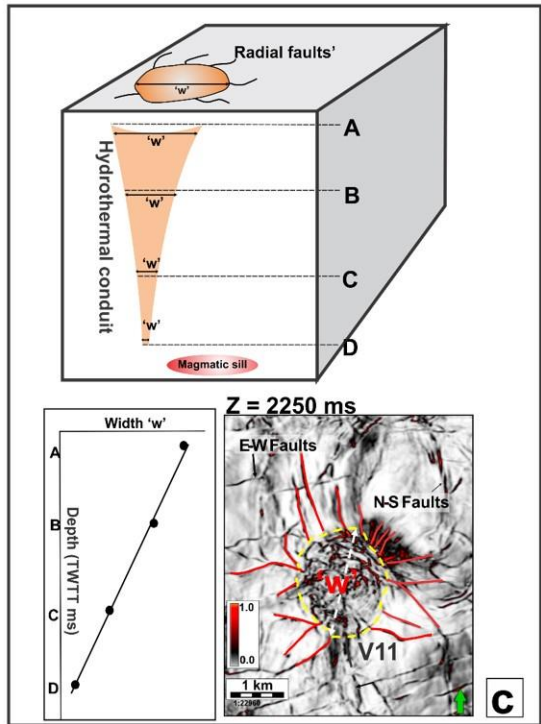
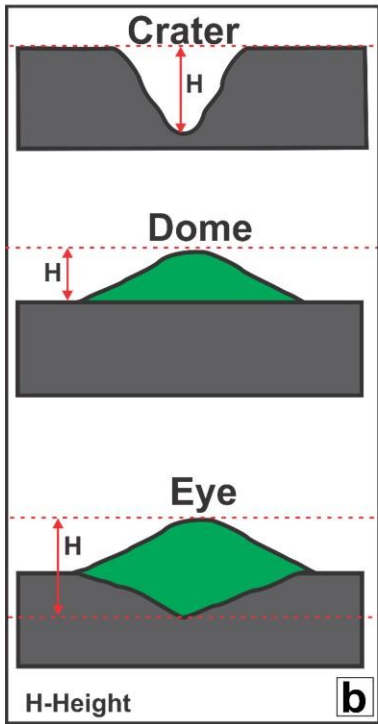
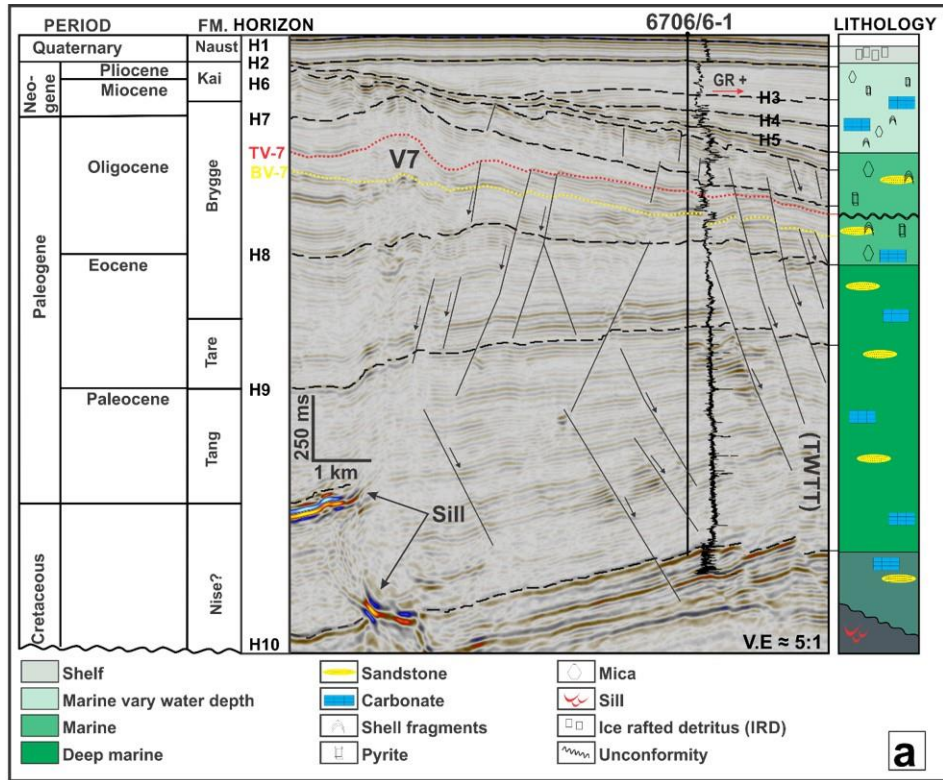
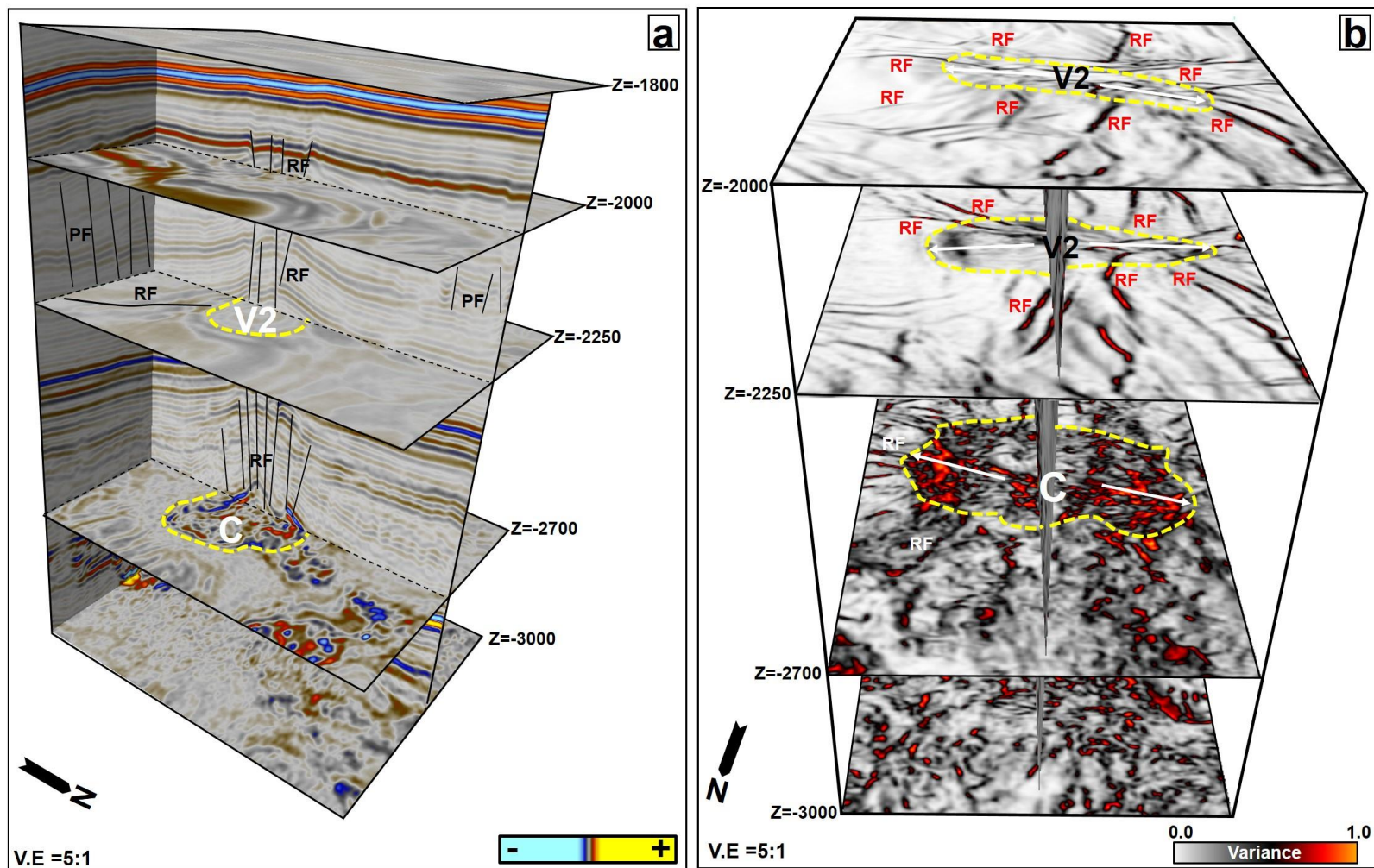


Figure 2: (a) Lithostratigraphy of the study area based on well 6706/6-1. The oldest unit intersected by borehole 6706/6-1 is the Cretaceous Nise Formation (b) The hydrothermal vent complex consists of an upper and a lower part. The upper part is crater-, dome-, or eye-shaped and is connected to the termination of a sill by a conduit zone (pipe) with disturbed seismic data (modified from Planke et al., 2005) (c) Schematic of typical hydrothermal vents on seismic data. In this study, the conduit width 'w' is measured on time slices or maps and corresponds to the longest axis marking the extent of the vents' conduits within the host-rock strata. By plotting conduit width with depth, a near perfect inverse linear relationship is expected for typical conical-shaped hydrothermal conduits. Also shown are examples of radial faults associated with V11. The white line shows the estimated width of the vents.



PF = Polygonal faults, RF = Radial faults, V= vents, C = Conduit

Figure 3: 3-D images showing the anatomy of a typical hydrothermal vent complex and the fault types discussed in the text. (a) 3-D image comprising seismic profiles and time slices where the vent and conduit are located. *The view is from the west.* (b) 3-D image comprised of variance time slices at depths where the hydrothermal vent complex in (a) is located. *The view is from the north.*

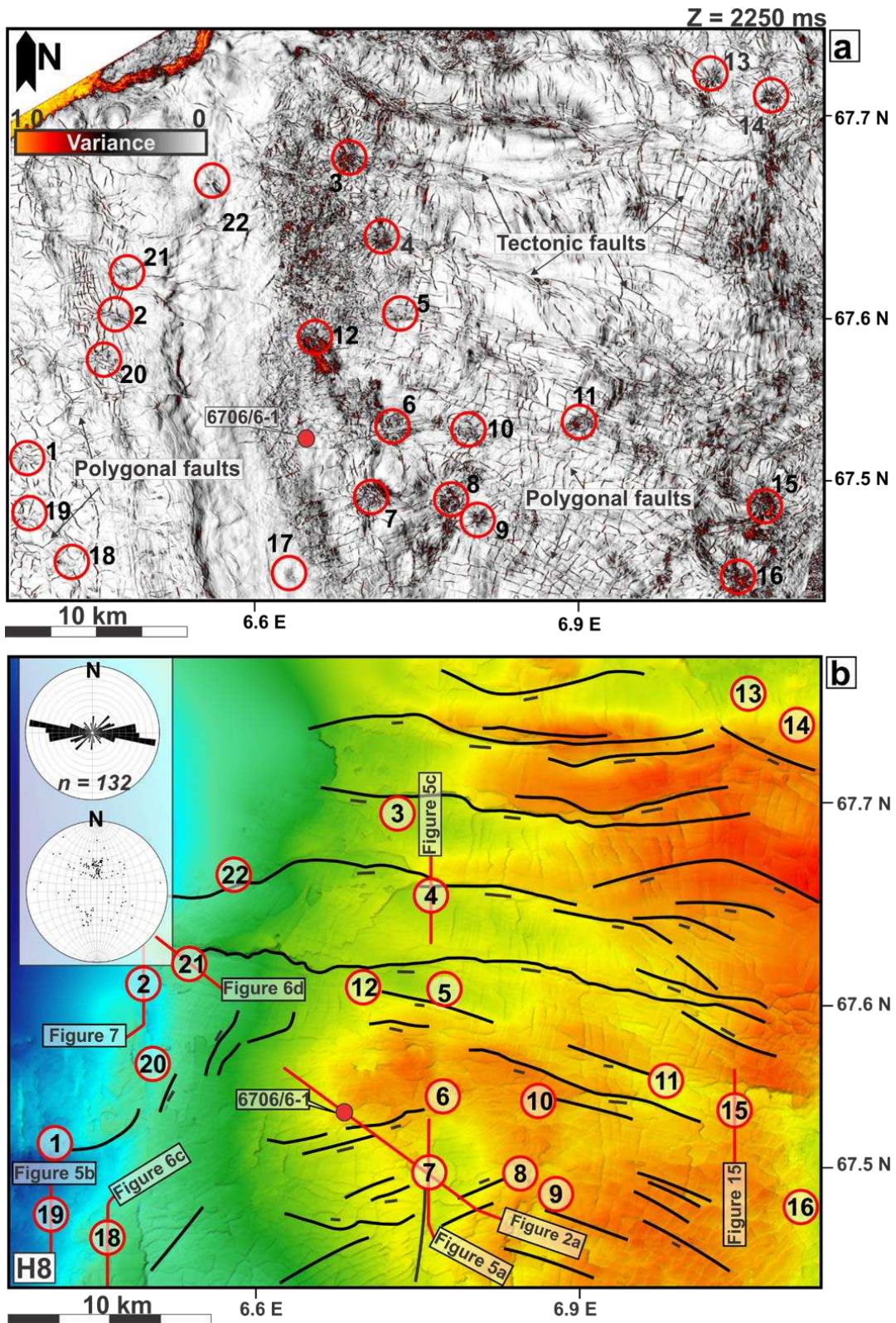


Figure 4: (a) Variance time slice at depth of 2250 ms showing a map view of some of the hydrothermal vents in relation to the tectonic and polygonal faults. (b) Structural maps on horizon H8 showing the location of the hydrothermal vent complexes and the principal tectonic faults interpreted in the study area. The inset shows a rose diagram and equal area plot for the faults.

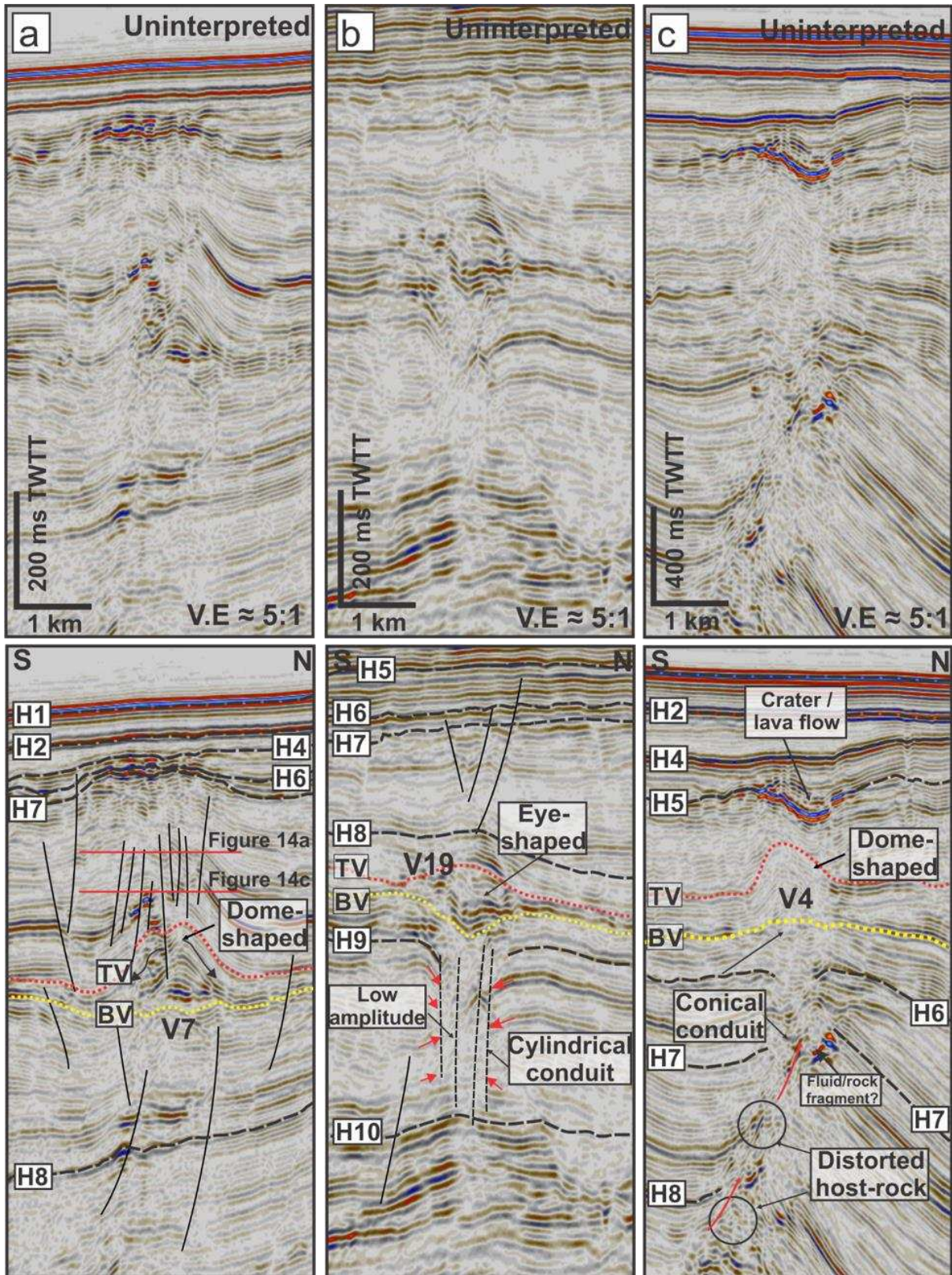


Figure 5: Examples of hydrothermal vents in the study area including (a) Dome-shaped (b) Eye-shaped and (c) Crater-shaped.

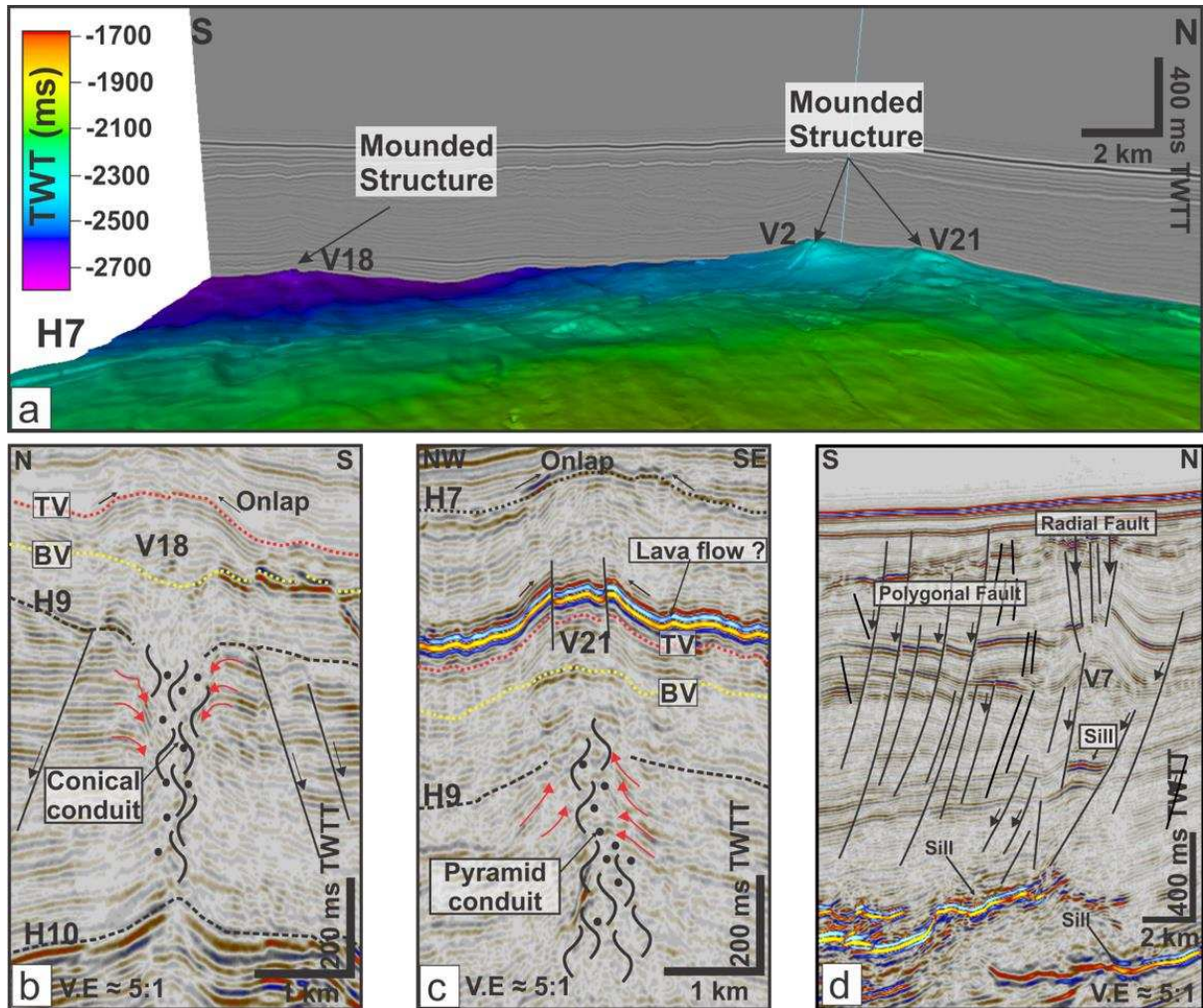


Figure 6: (a) Mound structures at the tops of V18, V2 and V21 (b) Structural map of Horizon H7 showing the location of the seismic sections in (b) and (c). Onlap reflections at the top of V18 and V21 provide a seismic stratigraphic indication of overburden uplift due to fluid expulsion during venting. The high amplitude reflection on top of V21 is interpreted as a lava flow. (d) Seismic section showing the connection between V7, polygonal faults and an underlying sill complex.

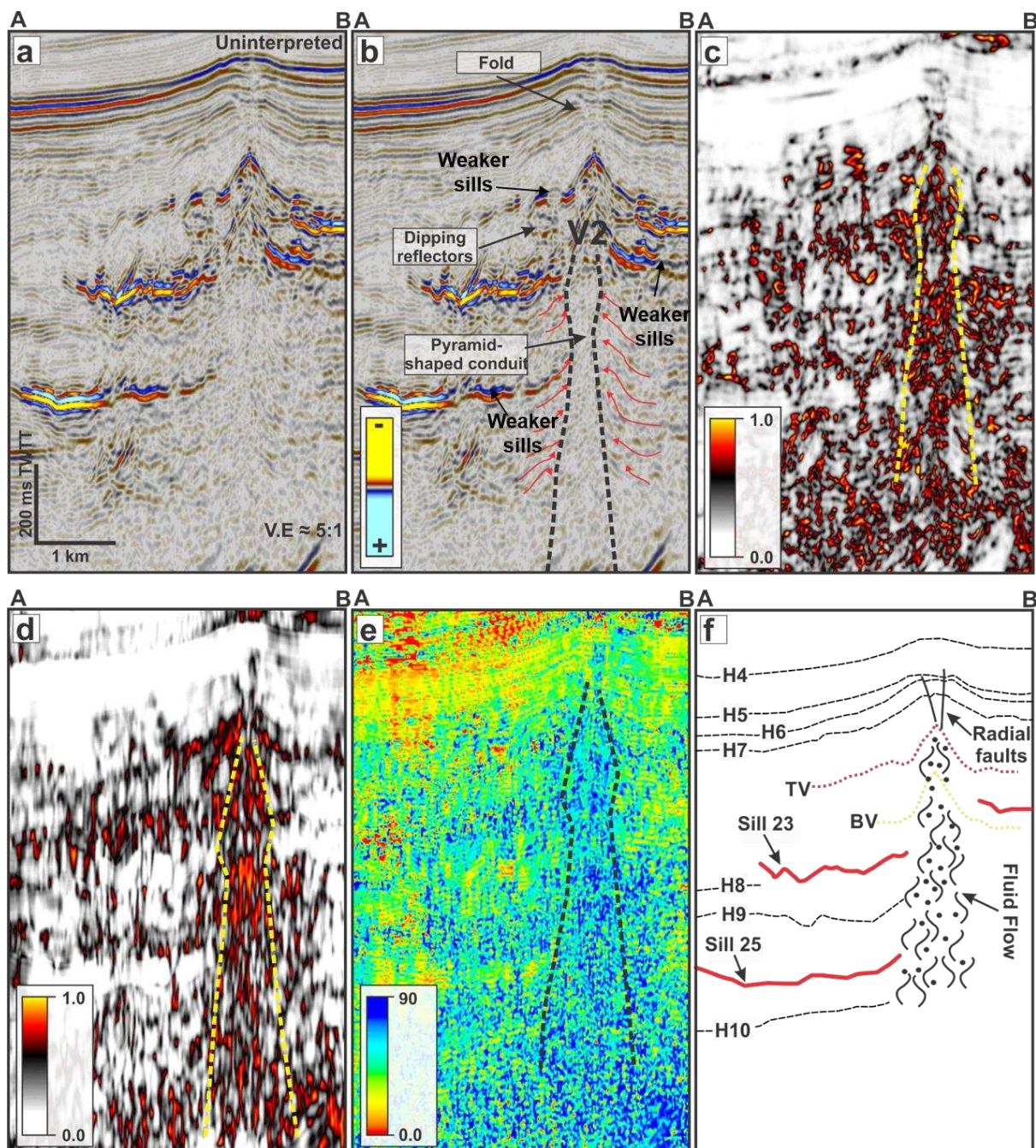


Figure 7: (a) and (b): Uninterpreted and interpreted seismic sections through V2. Also shown on the seismic sections are magmatic sills and vent conduits. (c) Chaos (d) Variance and (e) Local structural dip seismic attributes of the same section in (a). The interpreted geometry of the conduits is shown schematically in (F).

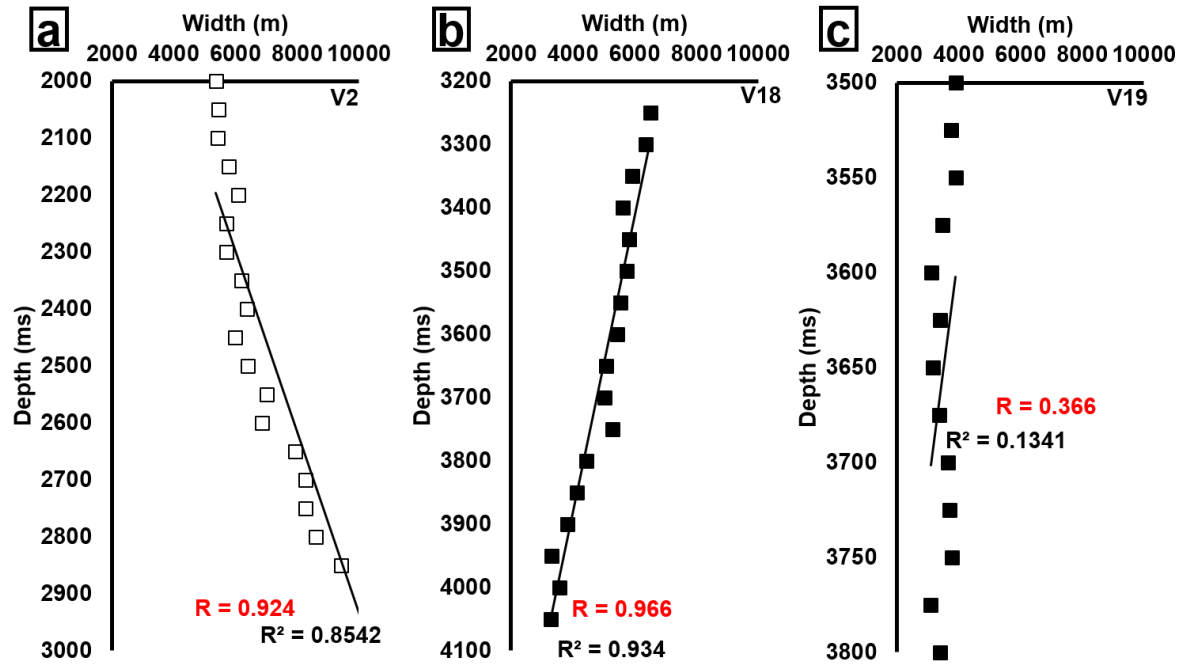


Figure 8: Examples of three end member plots for vent conduits' width versus depth including (a) increasing width with depth and (b) decreasing width with depth and (c) almost equal width of interference with depth.

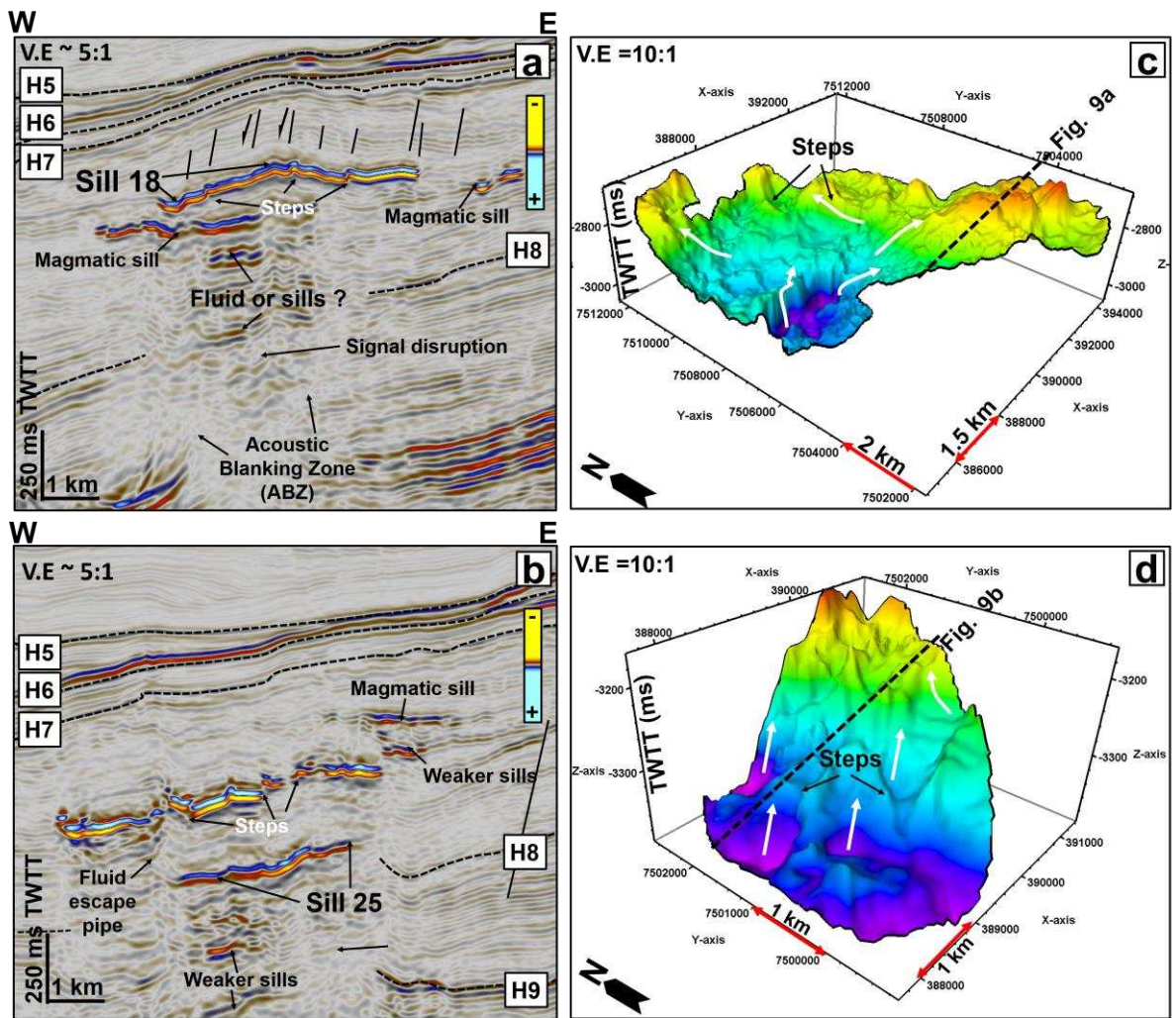


Figure 9: Seismic examples of magmatic sills in the study area (a) Sill 18 (b) Sill 25 structural map of a (c) saucer-shaped sill, e.g., Sill 18 and (d) a transgressive sill, e.g., Sill 25. Note: *The white arrows are flow indicators showing the inferred direction of magma transport.*

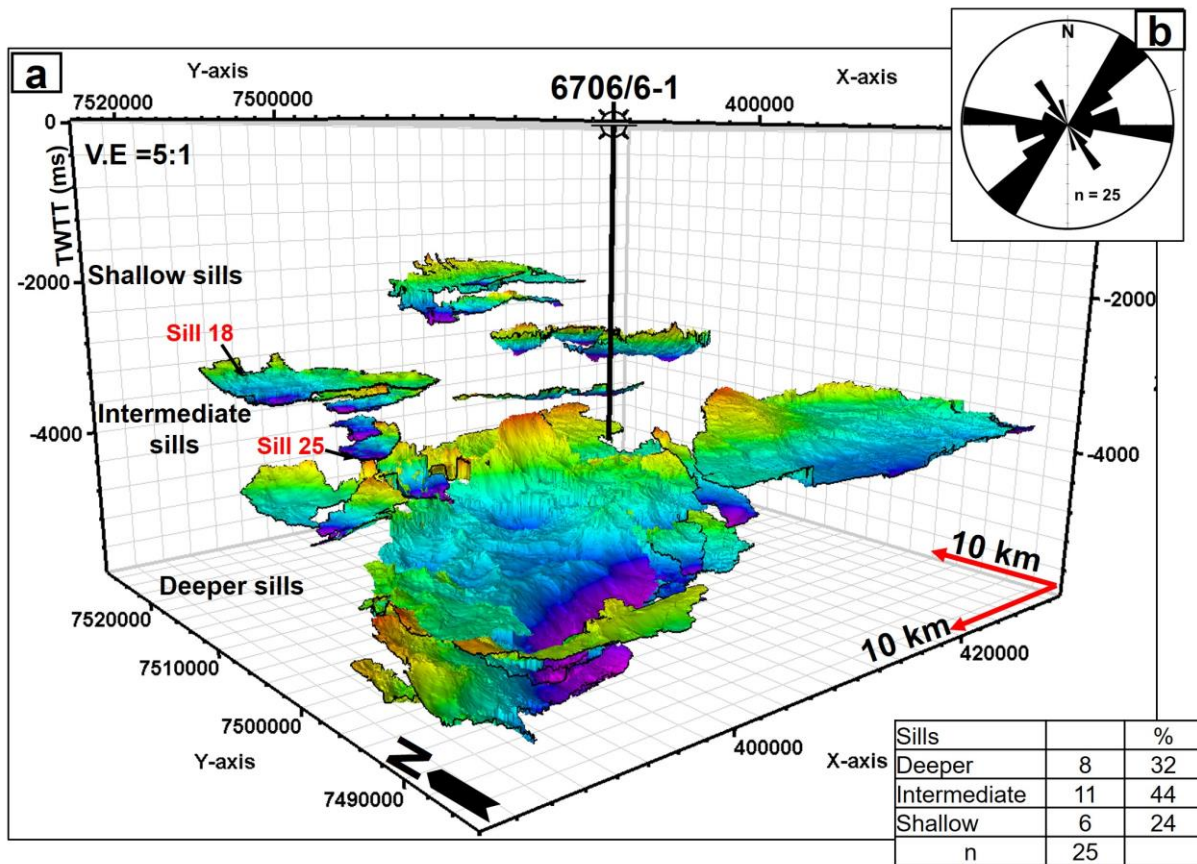


Figure 10: (a) Magmatic sills associated with hydrothermal vents in the study area are classified as deeper sills at depths of approximately 5800 ms TWTT, intermediate sills at depths of 4000 ms TWTT and shallow sills occurring at approximately 2500 ms TWTT (b) Rose diagram for the long axes of the magmatic sills.

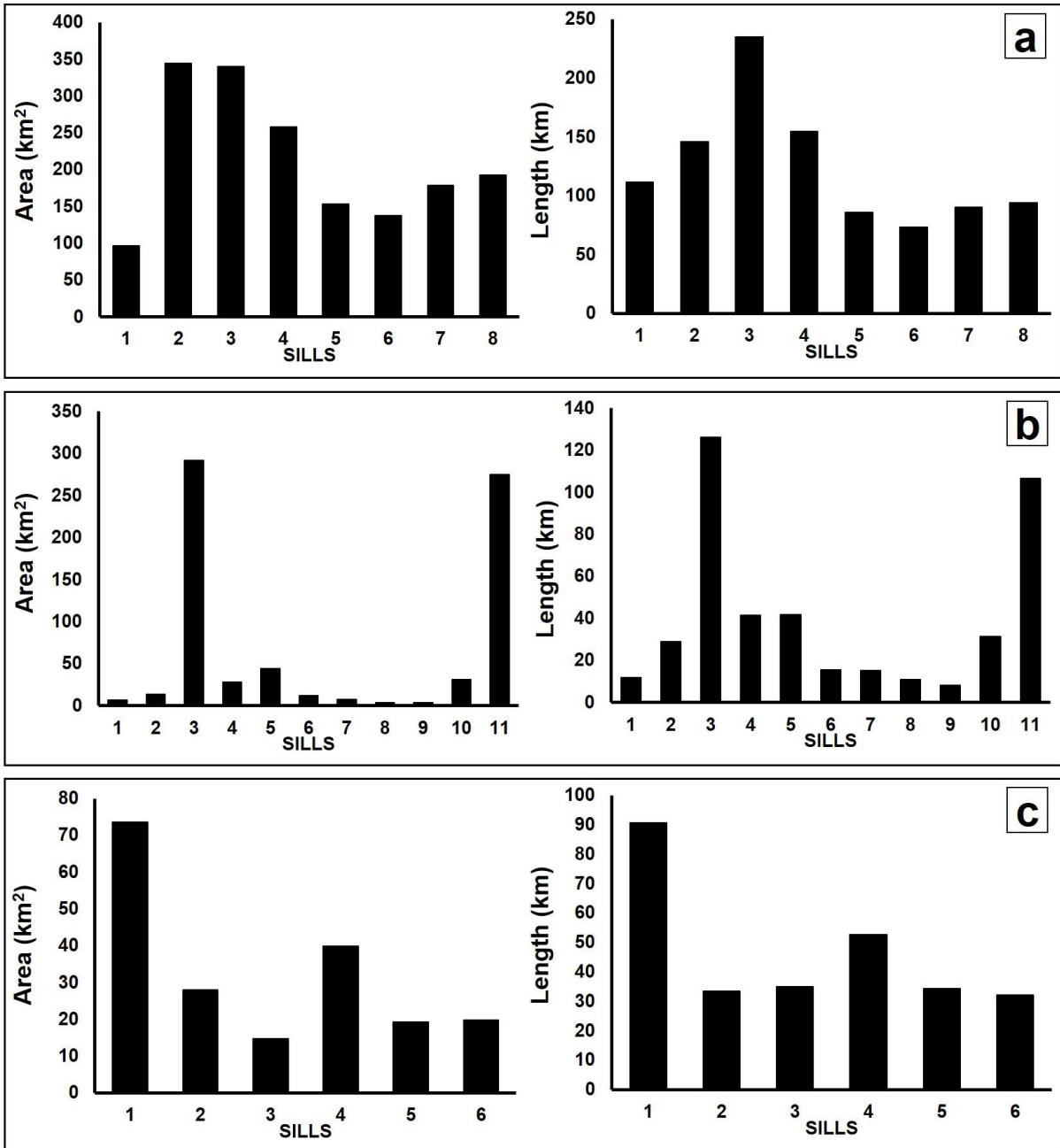


Figure 11: Bar charts showing the areas and lengths of (a) deeper sills (b) intermediate sills and (c) shallow sills. The deeper and intermediate sills have larger areas and lengths than the shallow sills.

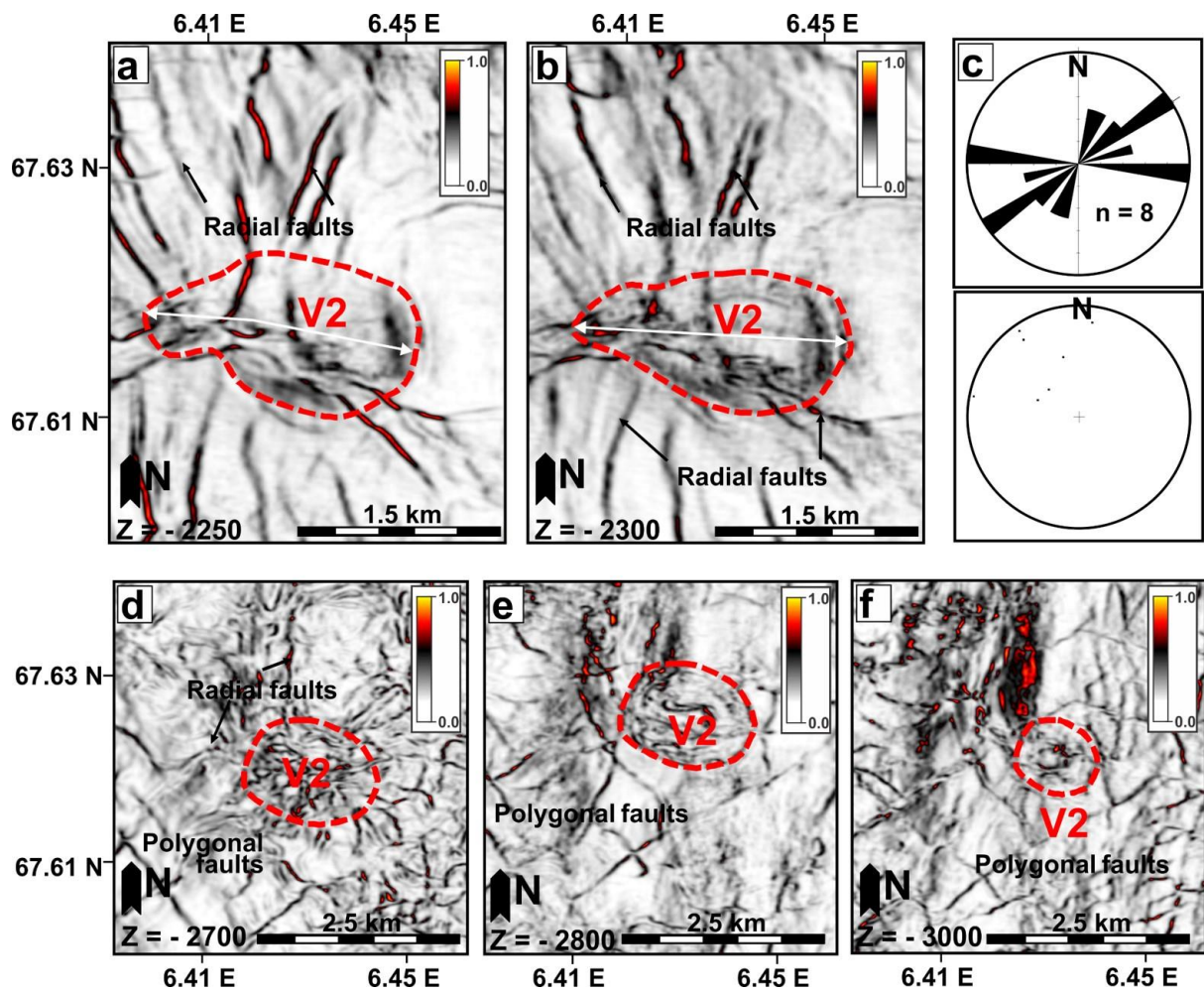


Figure 12: Variance slice through V2 showing (a) and (b) radial faults at the summit of V2 (c) Rose diagram and equal area plot for the orientation of the interpreted radial faults (d) to (f) Variation of fault types associated with the conduit of V2.

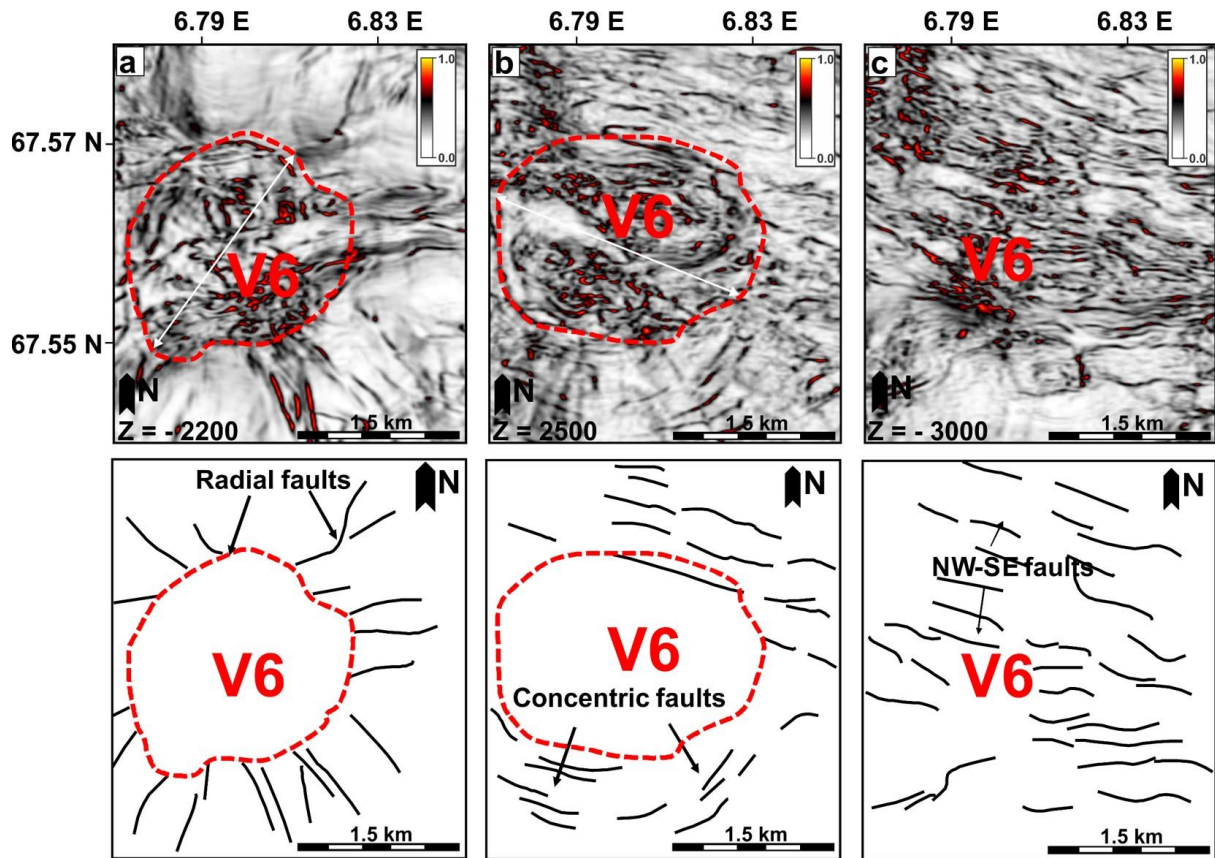


Figure 13: (a) - (c) Variance time slices showing the variation and changes in character of faults associated with V6 and its conduit. The fault types change from being radial faults at the summit of the vent to concentric faults and later NW-SE oriented faults.

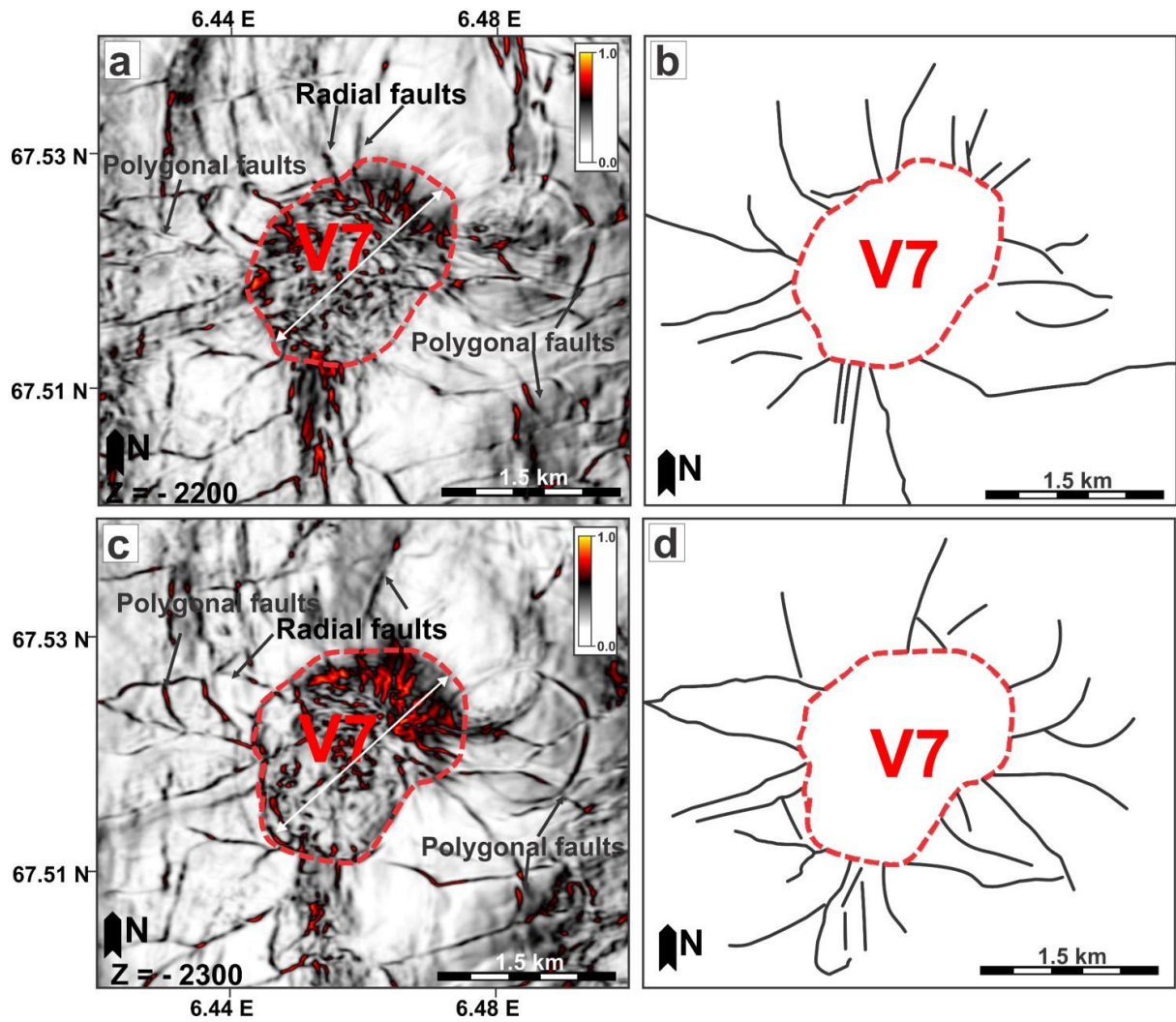


Figure 14: Variance slices showing examples of radial faults associated with V7. The radial faults frequently interact with polygonal faults at the summit of V7.

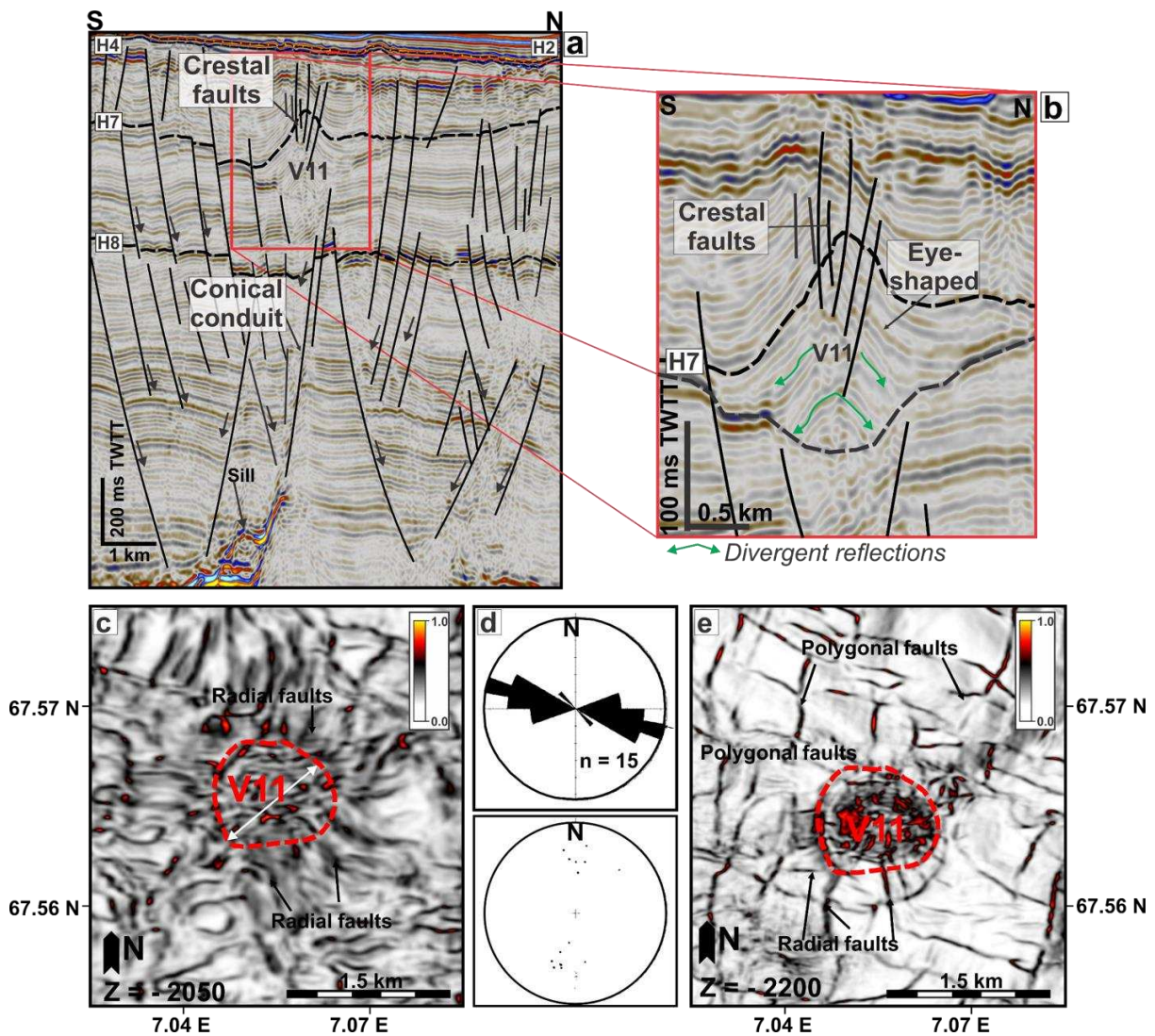


Figure 15: (a) and (b) Vent V1 and its associated fault types in seismic section. (c) Variance slice depth of 2050 ms showing the radial faults at the summit of the V11. (d) Rose diagram and equal area plot for the attitude of the interpreted radial faults at the summit of V11. (e) Variance slice at depth of 2200 ms showing faults associated with the conduit of V11.

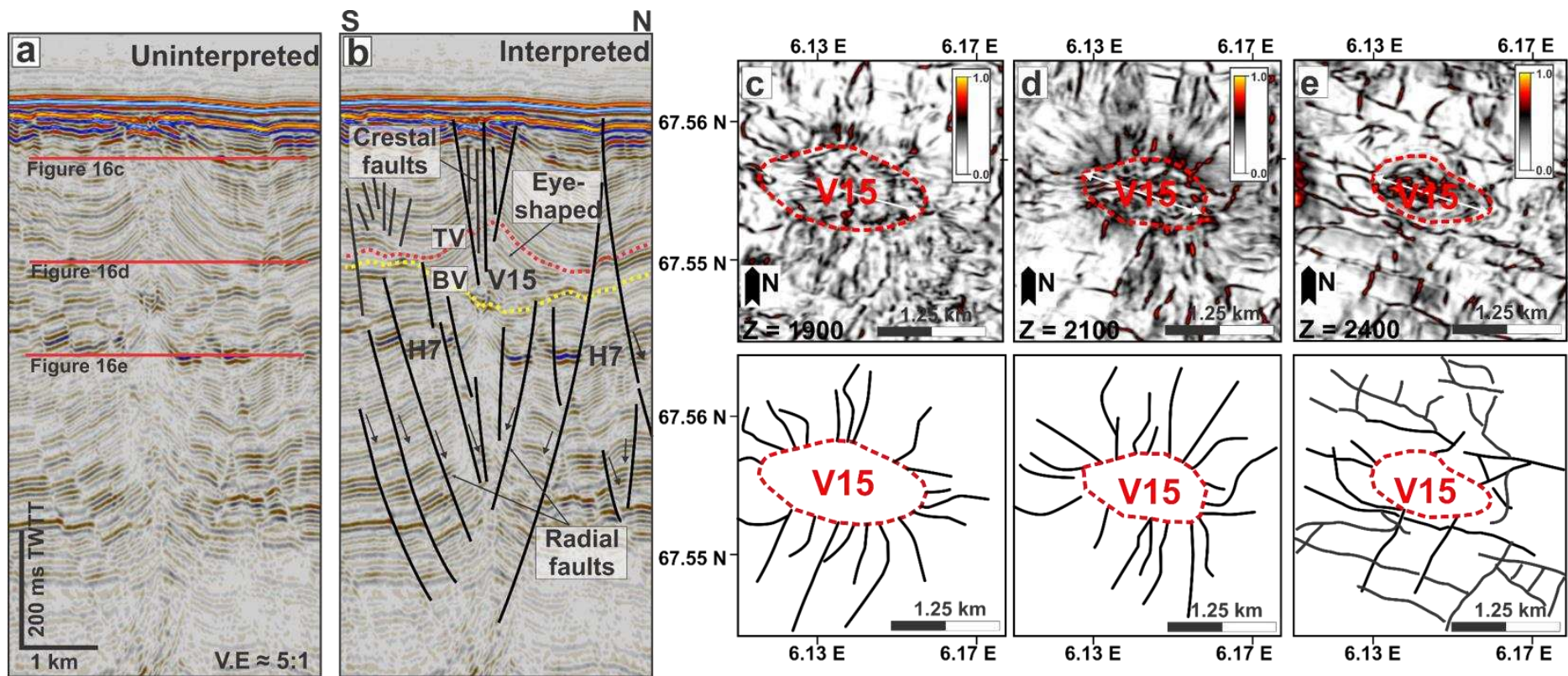


Figure 16: (a) and (b) Uninterpreted and interpreted seismic section showing an example of radial faults associated with V15. The faults occur on the flank of the vent conduit and also at the crest of the vent (c) to (e) Variance slice through the radial faults.

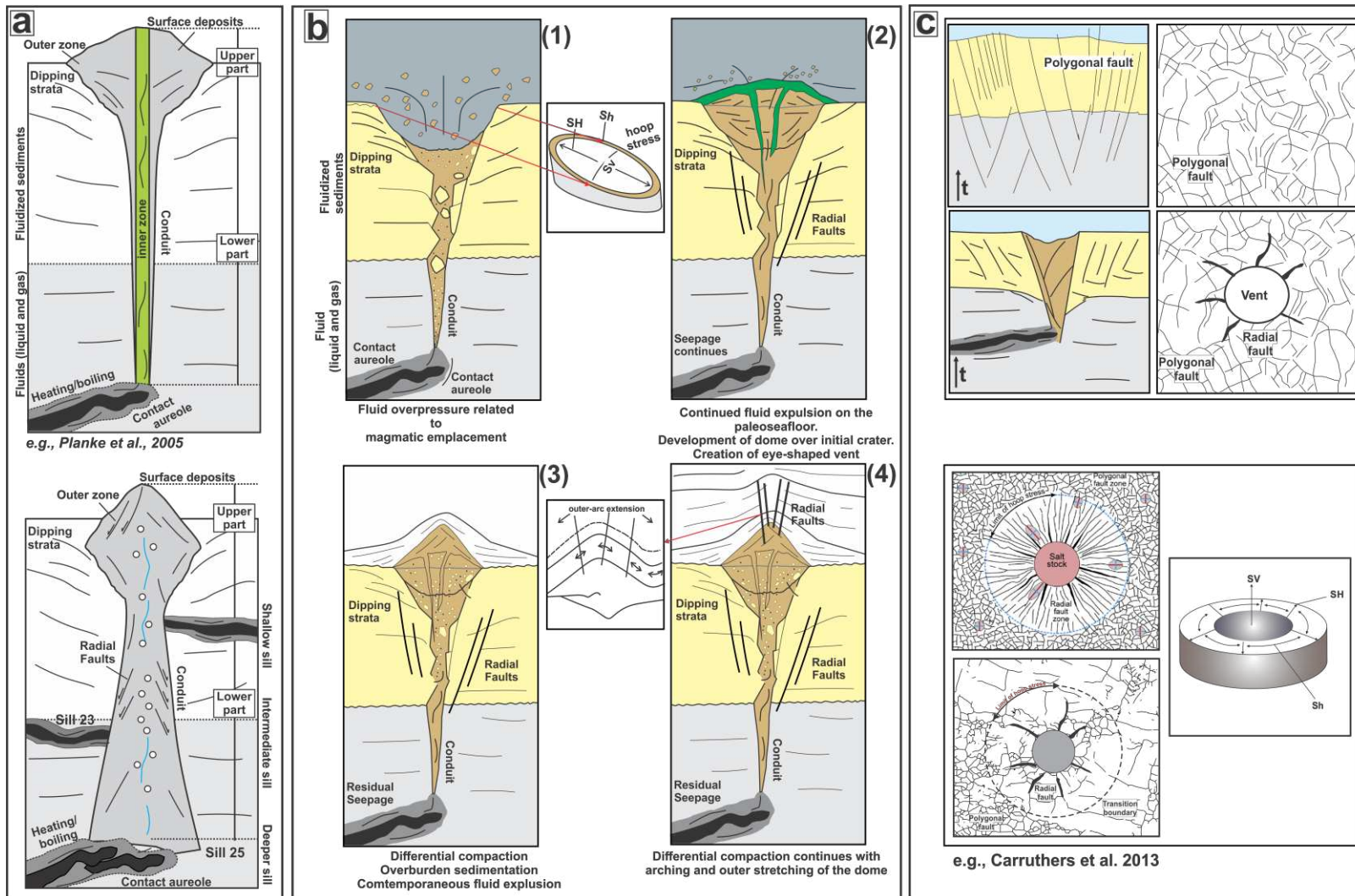


Figure 17: (a) Schematic representation of a typical hydrothermal vent complex from Planke et al., 2005 and pyramid-shaped conduits presented in this work. (b) Model I explaining the evolution of vent-related faults as compaction faults above dome-shaped vents. (c) Model II for the evolution of the vent-related radial faults above craters and eye-shaped vents. Analogues are documented in many salt-rich sedimentary basins.

1
2
3
4
5
6
7
8
9
10
11
12
13
14
15
16
17
18
19
20
21
22
23
24
25
26
27
28
29
30
31